JOURNAL OF PETROLOGY | VOLUME 49 | NUMBER 1 | PAGES 163–193 | 2008 | doi:10.1093/petrology/egm075

Origin and Evolution of Silicic Magmatism at Yellowstone Based on Ion Microprobe Analysis of Isotopically Zoned Zircons

ILYA N. BINDEMAN[1]*, BIN FU[2], NORIKO T. KITA[2] AND JOHN W. VALLEY[2]

[1]DEPARTMENT OF GEOLOGICAL SCIENCES, UNIVERSITY OF OREGON, EUGENE, OR 97403, USA

[2]DEPARTMENT OF GEOLOGY AND GEOPHYSICS, UNIVERSITY OF WISCONSIN, MADISON, WI 53706, USA

RECEIVED DECEMBER 19, 2006; ACCEPTED NOVEMBER 2, 2007
ADVANCE ACCESS PUBLICATION DECEMBER 4, 2007

The origin of large-volume Yellowstone ignimbrites and smaller-volume intra-caldera lavas requires shallow remelting of enormous volumes of variably ^{18}O-depleted volcanic and sub-volcanic rocks altered by hydrothermal activity. Zircons provide probes of these processes as they preserve older ages and inherited $\delta^{18}O$ values. This study presents a high-resolution, oxygen isotope examination of volcanism at Yellowstone using ion microprobe analysis with an average precision of ± 0·2‰ and a 10 μm spot size. We report 357 analyses of cores and rims of zircons, and isotope profiles of 142 single zircons in 11 units that represent major Yellowstone ignimbrites, and post-caldera lavas. Many zircons from these samples were previously dated in the same spots by sensitive high-resolution ion microprobe (SHRIMP), and all zircons were analyzed for oxygen isotope ratios in bulk as a function of grain size by laser fluorination. We additionally report oxygen isotope analyses of quartz crystals in three units. The results of this work provide the following new observations. (1) Most zircons from post-caldera low-$\delta^{18}O$ lavas are zoned, with higher $\delta^{18}O$ values and highly variable U–Pb ages in the cores that suggest inheritance from pre-caldera rocks exposed on the surface. (2) Many of the higher-$\delta^{18}O$ zircon cores in these lavas have U–Pb zircon crystallization ages that postdate caldera formation, but pre-date the eruption age by 10–20 kyr, and represent inheritance of unexposed post-caldera sub-volcanic units that have $\delta^{18}O$ similar to the Lava Creek Tuff. (3) Young and voluminous 0·25–0·1 Ma intra-caldera lavas, which represent the latest volcanic activity at Yellowstone, contain zircons with both high-$\delta^{18}O$ and low-$\delta^{18}O$ cores surrounded by an intermediate-$\delta^{18}O$ rim. This implies inheritance of a variety of rocks from high-$\delta^{18}O$ pre-caldera and low-$\delta^{18}O$ post-caldera units, followed by residence in a common intermediate-$\delta^{18}O$ melt prior to eruption. (4) Major ignimbrites of Huckleberry Ridge, and to a lesser extent the Lava Creek and Mesa Falls Tuffs, contain zoned zircons with lower-$\delta^{18}O$ zircon cores, suggesting that melting and zircon inheritance from the low-$\delta^{18}O$ hydrothermally altered carapace was an important process during formation of these large magma bodies prior to caldera collapse. (5) The $\delta^{18}O$ zoning in the majority of zircon core–rim interfaces is step-like rather than smoothly inflected, suggesting that processes of solution–reprecipitation were more important than intra-crystalline oxygen diffusion. Concave-downward zircon crystal size distributions support dissolution of the smaller crystals and growth of rims on larger crystals. This study suggests that silicic magmatism at Yellowstone proceeded via rapid, shallow-level remelting of earlier erupted and hydrothermally altered Yellowstone source rocks and that pulses of basaltic magma provided the heat for melting. Each post-caldera Yellowstone lava represents an independent homogenized magma batch that was generated rapidly by remelting of source rocks of various ages and $\delta^{18}O$ values. The commonly held model of a single, large-volume, super-solidus, mushy-state magma chamber that is periodically reactivated and produces rhyolitic offspring is not supported by our data. Rather, the source rocks for the Yellowstone volcanism were cooled below the solidus, hydrothermally altered by heated meteoric waters that caused low $\delta^{18}O$ values, and then remelted in distinct pockets by intrusion of basic magmas. Each packet of new melt inherited zircons that retained older age and $\delta^{18}O$ values. This interpretation may have significance for interpreting seismic data for crustal low-velocity zones in which magma mush and solidified areas experiencing hydrothermal circulation occur side by side. New basalt intrusions into this solidifying batholith are required to form the youngest volcanic rocks that erupted as independent rhyolitic magmas. We also suggest that the Lava Creek Tuff

*Corresponding author. E-mail: bindeman@uoregon.edu

Table 1: List of Yellowstone units and sample names analyzed in this study

Sample	Unit	Unit abbreviation	Eruption age (Ma)	U–Pb dating	$\delta^{18}O$ melt (‰)	Zr, WR (ppm)	*T* Zrc sat (°C)
CYCLE 1 Magmatism							
HRTB	Huckleberry Ridge Tuff, 2450 km^3, unit B	HRTB	2·04	same sample	*7·0*	328	863
HRTC	Huckleberry Ridge Tuff, 2450 km^3, unit C	HRTC	2·04	same sample	*7·5*	445	897
post HRT intracaldera lavas, > 50 km^3							
BC1	Blue Creek flow	BC	*1·75–1·78*	same spots	*2·9*	394	876
CYCLE 2 Magmatism							
MFT	Mesa Falls Tuff, 280 km^3	MFT	1·30	same sample	*5·4*	168	800
CYCLE 3 Magmatism							
LCT3a	Lava Creek tuff, unit A, 1000 km^3	LCT	0·64	same spots	*5·9*	186	825
Upper Basin lavas, post-LCT caldera, intracaldera, 70 km^3							
YL18	Canyon flow	CF	0·48	same spots	0·7	225	825
YL4	Dunraven Rd flow	DR	0·48	same spots	1·0	393	883
YL2	South Biscuit Basin flow	SBB	$0{\cdot}255 \pm 0{\cdot}011$*	n.d.	3·7	315	850
Central Plateau Member lavas, post-LCT caldera, intracaldera, 900 km^3							
YL20	Middle Biscuit Basin flow	MBB	0·52	same spots	1·1	204	826
YL9	Scaup Lake flow	SCL	0·20	n.d.	4·0	312	847
YL16	Solfatara Plateau flow	SP	0·11	same unit†	3·2	549	905

Eruption ages are derived from Ar–Ar (Gansecki *et al*. 1996; Lanphere *et al*. 2002); italics are K–Ar ages from Obradovich (1992); unit volumes are from Christiansen (2001).
*New data, this study. Analyses were performed at New Mexico Tech by incremental heating on sanidine (MSWD 0·6). n.d., not dated by U–Pb method; Zr, WR are Zr concentrations, T Zrc sat (zircon saturation temperature), and $\delta^{18}O$ melt are from Bindeman & Valley (2001). $\delta^{18}O$ melt values are for glass; italics are estimates based on feldspar phenocrysts. †Vazquez & Reid (2002).

magma was already an uneruptable mush by the time of the first post-caldera eruption after 0·1 Myr of the climactic caldera-forming eruption.

KEY WORDS: *Yellowstone; oxygen isotopes; geochronology; isotope zoning; zircon; U–Pb dating; caldera; rhyolite; ion microprobe*

INTRODUCTION

The Yellowstone Plateau Volcanic Field, which is one of the best examples of a complex and 'restless' caldera in the world, provides a classic example of a large-volume, planetary-scale silicic volcanic province (Smith, 1979). Voluminous eruptions of magma occurred violently in caldera-forming events, and more quietly as intra-caldera and extra-caldera lava flows (Table 1; Christiansen, 2001). Yellowstone caldera is the youngest of a series of large calderas that formed during sequential cataclysmic eruptions along the Snake River Plain that began 16 Myr ago in Oregon. Yellowstone volcanism occurred in three caldera cycles spanning 2·1 Myr (Fig. 1). Chemically similar, high-silica rhyolites erupted to form 300–2500 km^3 pyroclastic products of these caldera-forming eruptions [Huckleberry Ridge Tuff (Caldera 1, 2·04 Ma, 2500 km^3), Mesa Falls Tuff (Caldera 2, 1·3 Ma, 300 km^3), and Lava Creek Tuff (Caldera 3, 0·64 Ma, 1000 km^3)], and as post-caldera and intra-caldera lavas of comparable cumulative volumes (Christiansen, 2001).

The origin of such large volumes of silicic magma has been the subject of many geochemical and petrological studies. Highly enriched Sr, Pb, and Nd isotope ratios require tens of per cent of old upper crust to be incorporated into the volcanic products (Doe *et al.*, 1982; Leeman, 1982). Thus models involving differentiation of plume-related basalt must include partial melting of old continental crust (Hildreth *et al.*, 1991). Subsequent volcanism may recycle young volcanic products that variably inherit these enriched radiogenic isotope signatures.

We believe that the key evidence for the origin of magmas at Yellowstone comes from oxygen isotope ratios. Friedman *et al.* (1974), Hildreth *et al.* (1984, 1991), Taylor (1986), and Bindeman & Valley (2000, 2001) presented evidence that most of the *c.* 6000 km^3 of volcanic rocks are depleted in ^{18}O, thus requiring that meteoric water-derived oxygen be present in the magmas. Thus low-$\delta^{18}O$ values in the magmatic rocks serve as an important isotopic fingerprint of near-surface processes.

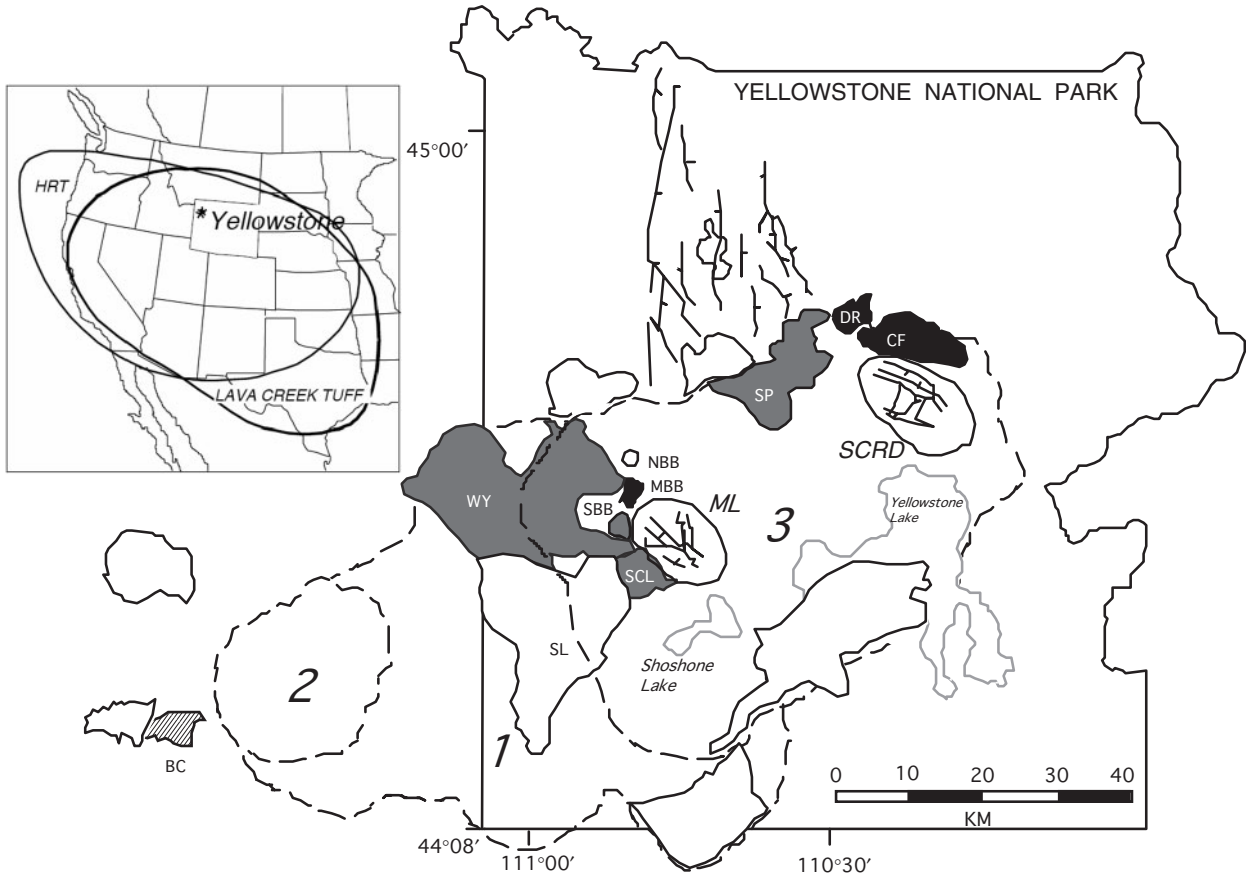

Fig. 1. Map of the Yellowstone Plateau Volcanic Field showing the inferred boundaries of the three calderas, selected lavas, and locations of analyzed units. Black shading indicates 0·5 Ma post-LCT Upper Basin Member lavas; gray shading indicates 0·25–0·1 Ma Central Plateau Member lavas; hatched pattern indicates post-HRT Blue Creek flow. ML and SCRD are the Mallard Lake and Sour Creek Resurgent Domes within the 0·64 Ma Yellowstone Caldera (3). 1, the Big Band caldera, which formed in response to the Huckleberry Ridge Tuff eruption at 2·04 Ma; 2, the Island Park caldera of the Mesa Falls Tuff eruption at 1·3 Ma. The inset shows the position of Yellowstone and the current ash distribution. Abbreviations for lava flows discussed in the text: BC, Blue Creek; SBB, MBB, and NBB are south, middle, and north Biscuit Basin flows; DR, Dunraven Road; CF, Canyon; SCL, Scaup Lake; WY, West Yellowstone; SP, Solfatara Plateau.

We concentrate on the post-Lava Creek Tuff (LCT) volcanic rocks because these units are the most $\delta^{18}O$ depleted and because the origin of the last cycle of volcanism since the LCT bears on the modern-day presence or absence of a large, slowly cooling, mushy-type magma body that earlier yielded the 1000 km^3 LCT at 0·64 Ma. Our new results constrain speculations about the beginning of a new magmatic cycle after the latest spike of intra-caldera volcanism at 0·25–0·1 Ma that might have relevance for prediction of future volcanic hazards (e.g. Wicks *et al.*, 2006).

The interpretations and conclusions about the petrogenesis of silicic magmas at Yellowstone may be applicable to similar settings where the O-isotope contrast between low-$\delta^{18}O$ meteoric waters and the magma is less dramatic. In particular, at Yellowstone and in other calderas and rift settings, low-$\delta^{18}O$ magmas signify shallow-level (typically 1–5 km), upper crustal petrogenesis, where meteoric hydrothermal systems developed within volcanic and sub-volcanic intra-caldera rocks that were subsequently remelted to form new rhyolitic magmas. Recognizing that mass balance and heat represent the ultimate constraints on the production of several per mil depletions in $\delta^{18}O$ values in magmas, many researchers including Hildreth *et al.* (1984, 1991), Taylor (1986), and Bacon *et al.* (1989) have debated the relative importance of direct influx of meteoric waters into the magma, exchange with stoped blocks and their pore fluids, and assimilation and partial melting of low-$\delta^{18}O$ hydrothermally altered wall-rocks.

Bindeman & Valley (2000, 2001) presented the following results for Yellowstone magmatism based on single-phenocryst oxygen isotope analysis of volcanic rocks spanning a period of 2·1 Myr (Fig. 2). Post-caldera lavas contain an isotopically diverse population of quartz and zircon phenocrysts that are zoned with respect to $\delta^{18}O$ by up to 5‰, with cores of larger zircons exhibiting higher,

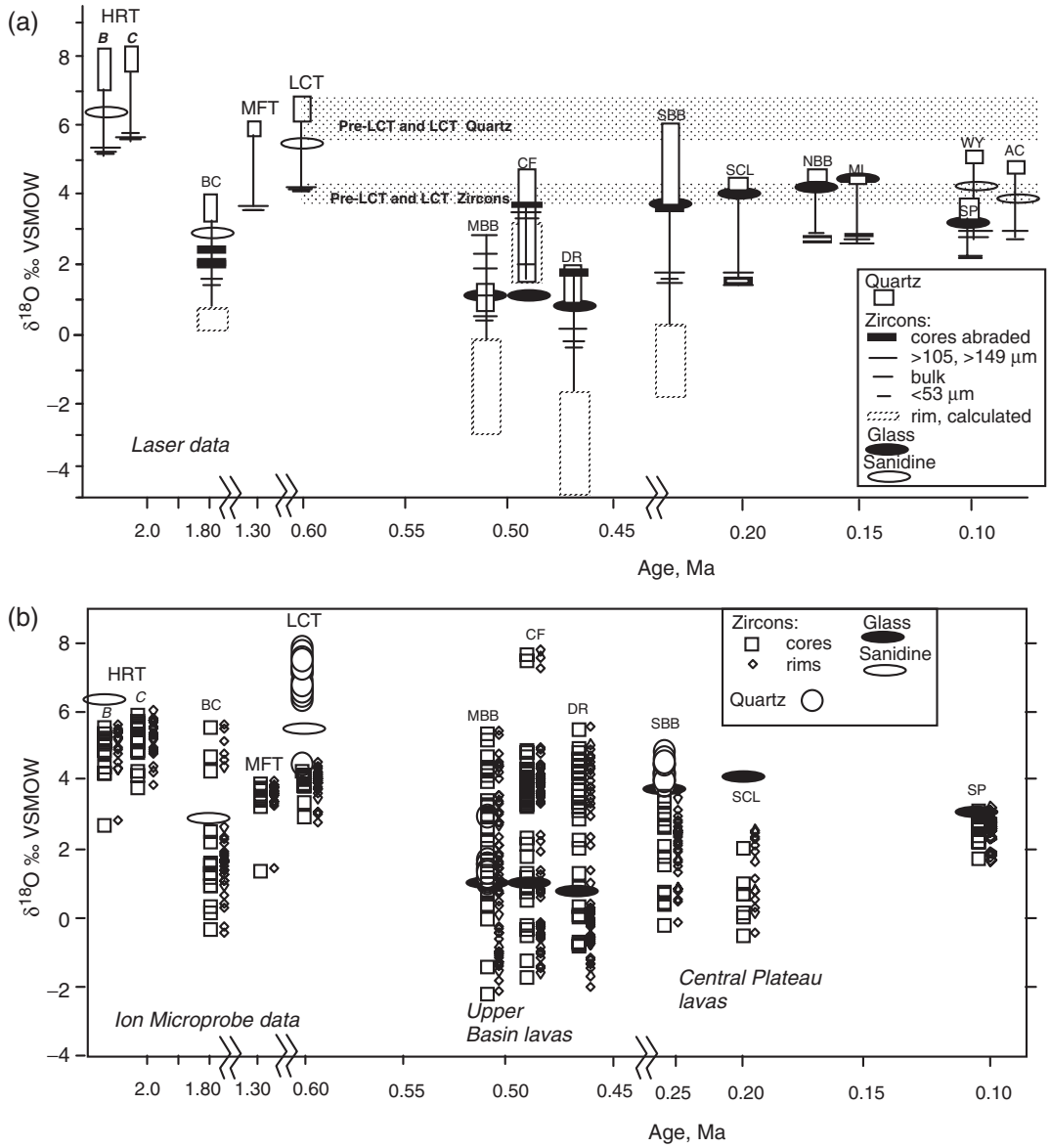

Fig. 2. Evolution of oxygen isotope ratios ($\delta^{18}O$ VSMOW) of zircons and quartz in Yellowstone magmas, with emphasis on post-Lava Creek Tuff intra-caldera volcanic rocks plotted vs Ar–Ar eruptive age. (a) Oxygen isotope ratios in zircons of different crystal size analyzed in bulk, and single grains of quartz, feldspar, and obsidian glass determined by laser fluorination analysis; data from Bindeman & Valley (2001). (b) *In situ* ion microprobe analyses of $\delta^{18}O$ in zircon cores and rims (Table 2). Quartz and melt (ovals) are shown. (See Table 1 for abbreviations of units and their Ar–Ar eruption ages.)

pre-caldera $\delta^{18}O$ values. These isotopically zoned crystals occur in a homogeneous low-$\delta^{18}O$ obsidian glass. Each post-caldera lava has a distinct obsidian $\delta^{18}O$ value, and a unique character of the isotopic zoning of quartz and zircon, suggesting that these lavas represent independent magma batches developed after remelting of hydrothermally altered silicic protoliths. *In situ* U–Pb dating of zircon [sensitive high-resolution ion microprobe (SHRIMP), Bindeman *et al.*, 2001] reveals that the cores of nearly the entire population of analyzed zircons are inherited and span ages from the inception of volcanism at Yellowstone at 2·1 Ma to the eruption age of the host lavas. In contrast, the rims are uniformly equilibrated with the host magmas.

Vazquez & Reid (2002) determined U/Th disequilibria crystallization ages by ion microprobe analysis of zircons in several of the youngest and most voluminous post-LCT rhyolites of the Central Plateau Member (eruption ages 250–70 ka, Table 1). Those workers found fewer inherited zircons at U–Th equilibrium, but with the majority of zircons having U/Th crystallization age many tens of thousands of years older that the Ar–Ar eruption age of their

host lavas. Vazquez & Reid (2002) suggested a model of a single, long-lived, LCT-like differentiating magma mush that lasted for over 0·2 Myr and periodically yielded high-silica differentiates, favoring this model over remelting of hydrothermally altered wall-rocks. No oxygen isotope data were employed in their interpretation.

In this study, we present results of *in situ* ion microprobe oxygen isotope analysis of isotopically zoned zircons that are spatially correlated to earlier SHRIMP dated spots and were analysed previously by laser fluorination. Given this new dataset, we re-examine our earlier interpretations and those of others of silicic magma genesis in the Yellowstone Plateau Volcanic Field.

SAMPLES AND METHODS

Samples and imaging

Table 1 presents a summary of results from the earlier work of Bindeman & Valley (2001) for oxygen isotope analysis of ~2 mg 'bulk' samples by laser fluorination, and Bindeman *et al.* (2001) for U–Pb SHRIMP ages. In this study, 10 μm spots on zircons were analyzed for $\delta^{18}O$ by ion microprobe. For the majority of the samples, imaged zircon grain mounts dated by SHRIMP allowed us to determine $\delta^{18}O$ values directly below the U–Pb pits, which were removed by light grinding and polishing. In each case, sample and crystal names were retained. The KIM-5 zircon standard ($\delta^{18}O = 5{\cdot}09‰$, Valley, 2003) was face-mounted in the center of the four zircon mounts that were repolished. Previous U–Pb pits and any implanted oxygen were completely removed by this process and no effect of old pits on new analyses for oxygen isotope ratios is seen. Polishing was performed using diamond films to ensure the maximum flatness of the mount and to minimize relief. Flatness is a critical condition for precise and accurate determination of $\delta^{18}O$. Cathodoluminescence (CL) imaging was performed on a CAMECA SX-100 electron microprobe at the University of Oregon before O-isotope analysis, and optical and back-scattered electron imaging of analyzed pits in crystals was performed following O-isotope analysis to ensure a lack of inclusions of glass or other minerals in these pits.

The CL-imaged zircon cores are typically in the geometrically central part of the crystal, but are occasionally off-center. A few broken crystals were analyzed and their cores were exposed; we avoided analyses of the broken edges because it is not known if the breakage occurred during zircon handling in the laboratory or in the magma. Rims are seen as zones 10–25 μm wide near the crystal edge, typically having a lighter grey colour and less zoned CL pattern (Table 2). However, in some cases, rims were indistinguishable from the cores by CL. The thickness of the rims varies on the different crystallographic faces of each crystal, being thicker on pyramidal tips, as expected from faster zircon growth along the *c*-axis. However, there is rather significant crystal-to-crystal variability in a single sample in the thickness of rims along both prisms and tips that should reflect differences in growth rates and time spent in contact with the new magma. Some crystals have rims that are less than 10 μm wide and thus were not analyzed. In Table 2 core/rim area refers to the region between the core and the rim and/or the part that represents an overlap of core and rim as seen by CL. In several cases, the 10 μm diameter ion microprobe beam was too large to resolve the zones. Therefore, 10 μm is the spatial limit of our interpretation. A few larger crystals record two episodes of overgrowth and cores of different generations can be identified; these crystals are imaged and identified below.

The majority of mounted crystals were sectioned by polishing through their prismatic faces. The mounts were ground before polishing and we estimate that the mounted crystals were ground and polished to remove 30–50 μm, or to the approximate middle of the majority of flat-lying crystals. However, because of variable crystal size, thickness of the rim, and variations in grinding and polishing, different crystals are exposed somewhat differently. In this respect, analyses of the central parts of some polished surfaces may not reach the true center of the crystal.

All analyzed crystals had their width and length recorded, as well as CL intensity (Table 2). Because we targeted primarily larger grains with cores for both the U–Pb and oxygen isotope analysis, the analyzed crystal population is skewed toward larger crystal sizes, although a few smaller zircons were analyzed (Table 2). In general, the compositions of smaller zircons are represented by the outer zones of larger crystals. We also report ion microprobe analyses of 29 quartz crystals in units LCT, MBB, and SBB from Cycle 3 (Table 1) performed on separate mounts using the UWQ-1 standard with a $\delta^{18}O$ value of 12·35‰, which corresponds to a value of 9·6‰ for NBS-28 (Kelly *et al.*, 2007), and using the same analytical conditions as outlined below.

Methods of ion microprobe oxygen isotope analysis

The $^{133}Cs^{+}$ primary ion beam (20 keV total acceleration voltage) was focused to a diameter of 10 μm on the sample surface, and the secondary O^{-} ions were accelerated by −10 kV under the electron gun for charge compensation. The primary ion intensities were ~2 nA. The secondary optics are similar to those of Kita *et al.* (2004, 2007) and Kelly *et al.* (2007), which aim to achieve high secondary ion transmission. Detailed alignment includes: transfer lens magnification of 200, contrast aperture (CA) 400 mm diameter, field aperture (FA) 4000 μm × 4000 μm square, entrance slit 122 μm width, energy slit 40 eV width, and exit slit width 500 μm. At these conditions, both primary ion spot transferred to FA and the crossover image through the CA and entrance slit were almost fully transmitted.

Table 2: $\delta^{18}O$ values, age, U and Th concentrations, cathodoluminescence (CL) character, and sizes of zircons in studied units from Yellowstone

Crystal/spot	Core/rim	$\delta^{18}O \pm 1SD$	CL	Length (μm)	Width (μm)	Age core (Ma)	U (ppm)	Th (ppm)
Sample YL96-2 South Biscuit Basin, post-LCT (10 crystals, 28 spots)								
YL2-1-1	C	**2·10** ± 0·24	D	127	73			
YL2-1-2	R	**2·54** ± 0·24	L					
YL2-2-1	C	**2·70** ± 0·20	D	195	135			
YL2-2-2	R	**2·32** ± 0·20	G					
YL2-2-3	R	**1·63** ± 0·20	G					
YL2-3-1	C	**3·39** ± 0·20	G	160	95			
YL2-3-2	R	**0·76** ± 0·20	L					
YL2-3-3	C/R	**1·79** ± 0·20	G					
YL2-4-1	C	**2·69** ± 0·24	D	170	105			
YL2-4-2	R	**1·87** ± 0·24	L					
YL2-5-1	C	**3·58** ± 0·24	G	420	110			
YL2-5-2	R	**2·13** ± 0·24	G					
YL2-6-1	C	**1·55** ± 0·24	D	215	70			
YL2-6-2	R	**2·37** ± 0·24	L					
YL2-7-1	C	**3·08** ± 0·20	G	150	80			
YL2-7-2	R	**1·42** ± 0·20	G					
YL2-7-3	C/R	**2·86** ± 0·20	G					
YL2-7-4	R	**2·00** ± 0·20	G					
YL2-52-1	C	**−0·20** ± 0·20	G	300	105			
YL2-52-2	C	**0·44** ± 0·20	G					
YL2-52-3	R	**2·39** ± 0·20	G					
YL2-58-1	C	**0·73** ± 0·20	D	260	110			
YL2-58-2	R	**1·22** ± 0·20	L					
YL2-58-3	R	**2·45** ± 0·20	L					
YL2-59-1	C	**0·36** ± 0·24	D	300	140			
YL2-59-2	R	**2·48** ± 0·24	G					
YL2-59-3	R	**2·24** ± 0·24	G					
YL2-59-4	C	**0·80** ± 0·24	D					
Sample YL96-20, Middle Biscuit Basin, post-LCT (13 crystals, 60 spots)								
YL20-1-1	C	**3·44** ± 0·15	D	190	77			
YL20-1-2	R	**−1·34** ± 0·15	L					
YL20-1-3	R	**−1·16** ± 0·15	G					
YL20-1-4	C	**4·14** ± 0·15	D					
YL20-2-1	C	**2·64** ± 0·15	D	150	75	2·16 ± 0·05	5359	6141
YL20-2-3	R	**2·03** ± 0·15	G			2·16 ± 0·05		
YL20-2-4	R	**2·63** ± 0·15	G			2·16 ± 0·05		
YL20-2-5	R	**3·46** ± 0·15	L			2·16 ± 0·05		
YL20-2-6	C	**1·05** ± 0·20	D			2·16 ± 0·05		
YL20-2-7	R	**4·30** ± 0·20	L			2·16 ± 0·05		
YL20-3-1	C	**2·01** ± 0·19	D	180	90	0·61 ± 0·02	3920	4773
YL20-3-4	R	**1·76** ± 0·19	G			0·61 ± 0·02		
YL20-3-5	R	**1·37** ± 0·20	L			0·61 ± 0·02		
YL20-3-6	R	**−0·36** ± 0·20	L			0·61 ± 0·02		

(continued)

Table 2: Continued

Crystal/spot	Core/rim	$\delta^{18}O \pm 1SD$	CL	Length (μm)	Width (μm)	Age core (Ma)	U (ppm)	Th (ppm)
YL20-3-7	C	**1·39** ± 0·20	D			0·61 ± 0·02		
YL20-4-1	C	**−0·02** ± 0·19	D			0·86 ± 0·23	3604	2514
YL20-4-2	R	**−0·94** ± 0·19	L			0·86 ± 0·23		
YL20-5-1	C	**−1·43** ± 0·19	D	110	60	1·83 ± 0·1	1881	738
YL20-5-2	R	**−1·07** ± 0·19	L			1·83 ± 0·1		
YL20-6-1	C	**2·90** ± 0·22	D	140	75	0·58 ± 0·02	5618	6667
YL20-6-2	R	**−0·74** ± 0·22	G			0·58 ± 0·02		
YL20-6-3	R	**−1·49** ± 0·22	G			0·58 ± 0·02		
YL20-6-4	R	**−0·50** ± 0·22	G			0·58 ± 0·02		
YL20-6-5	C	**3·25** ± 0·22	D			0·58 ± 0·02		
YL20-6-6	R	**−1·13** ± 0·22	L			0·58 ± 0·02		
YL20-7-1	C	**3·00** ± 0·22	D	160	60	0·77 ± 0·05	2015	1402
YL20-7-2	R	**1·18** ± 0·22	L					
YL20-8-1	C	**1·57** ± 0·22	D	180	80	0·62 ± 0·04	3828	1664
YL20-8-2	R	**1·46** ± 0·22	L			0·62 ± 0·04		
YL20-9-1	C	**4·43** ± 0·22	G	150	80	0·59 ± 0·04	1041	467
YL20-9-2	R	**−1·65** ± 0·22	L			0·59 ± 0·04		
YL20-9-3	R	**1·01** ± 0·22	L			0·59 ± 0·04		
YL20·10-1	R	**−0·51** ± 0·15	G	165	65	0·63 ± 0·06		
YL20·10-2	C	**−2·24** ± 0·15	D			0·63 ± 0·06	4364	770
YL20·11-1	C	**3·93** ± 0·15	D	145	80	0·69 ± 0·03	2080	1295
YL20·11-2	C	**0·40** ± 0·15	D			0·69 ± 0·03		
YL20·11-3	R	**0·67** ± 0·15	L			0·69 ± 0·03		
YL20·11-4	C	**4·27** ± 0·15	G			0·69 ± 0·03		
YL20·11-5	R	**−1·90** ± 0·15	R			0·69 ± 0·03		
YL20·11-6	R	**−1·38** ± 0·15	G			0·69 ± 0·03		
YL20·11-7	C	**3·28** ± 0·15	G			0·69 ± 0·03		
YL20·11-8	R	**0·62** ± 0·15	L			0·69 ± 0·03		
YL20·11-9	C	**0·71** ± 0·15	D			0·69 ± 0·03		
YL20·12-2	C	**2·99** ± 0·19	G	270	95	0·89 ± 0·02	3977	3385
YL20·12-3	R	**−1·11** ± 0·19	L			0·89 ± 0·02		
YL20·12-4	R	**0·24** ± 0·19	L			0·89 ± 0·02		
YL20·12-5	R	**−0·40** ± 0·19	D			0·89 ± 0·02		
YL20·12-6	C	**2·24** ± 0·19	G			0·89 ± 0·02		
YL20·12-7	R	**−1·25** ± 0·19	G			0·89 ± 0·02		
YL20·12-8	C	**2·61** ± 0·19	G			0·89 ± 0·02		
YL20·12-9	R	**−1·03** ± 0·19	L			0·89 ± 0·02		
YL20·12-10	R	**−0·51** ± 0·19	L			0·89 ± 0·02		
YL20·12-11	C/R	**1·66** ± 0·19	G			0·89 ± 0·02		
YL20·12-12	C/R	**0·82** ± 0·19	G/D			0·89 ± 0·02		
YL20·13-1	C/R	**4·35** ± 0·22	G					
YL20·13-2	C	**5·19** ± 0·22	G				3365	2860
YL20·13-3	C	**5·30** ± 0·22	G					
YL20·13-4	C/R	**4·69** ± 0·22	L					

(continued)

Table 2: Continued

Crystal/spot	Core/rim	$\delta^{18}O \pm 1SD$	CL	Length (μm)	Width (μm)	Age core (Ma)	U (ppm)	Th (ppm)
Sample YL96-4 Dunraven Road flow, post LCT (13 crystals, 53 spots)								
YL4·1-1	C	**3·70** ± 0·14	D	210	75	2·00 ± 0·14	899	445
YL4·1-2	C	**3·39** ± 0·14	D			2·00 ± 0·14		
YL4·1-3	R	**0·00** ± 0·14	L			2·00 ± 0·14		
YL4·1-4	R	−**0·11** ± 0·14	L			2·00 ± 0·14		
YL4·1-5	C	**3·58** ± 0·14	L			2·00 ± 0·14		
YL4·2-1	R	−**0·35** ± 0·14	L	160	45	2·17 ± 0·07		
YL4·2-2	C	**4·39** ± 0·14	D			2·17 ± 0·07	1724	982
YL4·2-3	C	−**0·68** ± 0·14	D			2·17 ± 0·07		
YL4·2-4	C	**5·43** ± 0·14	G			2·17 ± 0·07	423	197
YL4·3-1	C/R	**4·06** ± 0·23	D	450	165	0·59 ± 0·10	357	235
YL4·3-2	C	−**0·82** ± 0·23	L				293	197
YL4·3-3	R	−**0·76** ± 0·23	L					
YL4·3-4	R	−**0·66** ± 0·23	L					
YL4·3-5	C	**3·91** ± 0·23	D					
YL4·3-6	C	**3·37** ± 0·23	D					
YL4·3-7	R	−**0·65** ± 0·23	G					
YL4·3-8	R	−**0·72** ± 0·23	L					
YL4·3-9	C	**4·19** ± 0·23	D					
YL4·3-10	C	**1·32** ± 0·23	D					
YL4·3-11	R	−**1·21** ± 0·23	L					
YL4·3-13	R	−**0·56** ± 0·23	G					
YL4·3-14	R	−**0·20** ± 0·23	G					
YL4·4-1	C	**4·96** ± 0·23	G	270	90	1·04 ± 0·17	184	143
YL4·4-2	R	−**1·75** ± 0·23	L			1·04 ± 0·17		
YL4·4-3	C	**4·78** ± 0·23	D			1·04 ± 0·17		
YL4·4-4	R	−**0·69** ± 0·23	L			1·04 ± 0·17		
YL4·5-1	C	**2·24** ± 0·17	D			0·65 ± 0·02	4784	7071
YL4·5-2	R	−**0·83** ± 0·17	G			0·65 ± 0·02		
YL4·5-3	C	**2·01** ± 0·17	G			0·65 ± 0·02		
YL4·5-4	R	−**0·78** ± 0·17	G			0·65 ± 0·02		
YL4·5-5	R	−**0·26** ± 0·17	G			0·65 ± 0·02		
YL4·5-6	R	−**0·82** ± 0·17	G			0·65 ± 0·02		
YL4·6-1	C	**0·92** ± 0·17	D	175	80	0·53 ± 0·06	4418	715
YL4·6-2	R	**0·19** ± 0·17	G			0·53 ± 0·06		
YL4·7-1	C	−**0·75** ± 0·14	D	125	95	0·54 ± 0·02	8140	9590
YL4·7-2	R	−**1·57** ± 0·14	L			0·54 ± 0·02		
YL4·8-1	C	**4·20** ± 0·17	G	250	80	3·52 ± 0·20	275	164
YL4·8-2	C/R	**2·84** ± 0·17	G			3·52 ± 0·20		
YL4·8-3	C/R	**4·28** ± 0·17	G			3·52 ± 0·20		
YL4·9-1	C	**0·05** ± 0·17	G	110	60	0·49 ± 0·14	154	126
YL4·9-2	R	−**1·44** ± 0·17	G			0·49 ± 0·14		
YL4·10-1	C	**0·34** ± 0·14	D	145	65	0·59 ± 0·05	4770	4407
YL4·11-1	C	**4·63** ± 0·23	G	550	120	0·75 ± 0·13	199	122
YL4·11-2	R	**0·17** ± 0·23	G			0·75 ± 0·13		
YL4·12-1	C	**3·11** ± 0·23	G	100	78			

(continued)

Table 2: Continued

Crystal/spot	Core/rim	$\delta^{18}O \pm 1SD$	CL	Length (μm)	Width (μm)	Age core (Ma)	U (ppm)	Th (ppm)
YL4-12-2	R	**−0·06** ± 0·23	G					
YL4-13-1	C	**3·23** ± 0·17	G	270	100	0·87 ± 0·06	672	289
YL4-13-2	R	**−1·31** ± 0·17	G			0·87 ± 0·06		
YL4-13-3	R	**−0·63** ± 0·17	G			0·87 ± 0·06		
YL4-13-4	C	**4·53** ± 0·17	G			0·87 ± 0·06		
YL4-13-5	C	**3·73** ± 0·17	G			0·87 ± 0·06		
YL4-13-1-6	R	**−1·41** ± 0·17	G			0·87 ± 0·06		
YL4-13-1-7	C/R	**0·11** ± 0·17	D			0·87 ± 0·06		
Sample YL96-18 Canyon flow, post-LCT (22 crystals 60 spots)								
YL18-1-1	C	**3·60** ± 0·15	G	310	120	0·50 ± 0·02	4219	4064
YL18-1-2	C/R	**3·36** ± 0·15	D			0·50 ± 0·02		
YL18-2-1	C	**3·82** ± 0·26	G	280	90			
YL18-2-2	R	**−0·31** ± 0·26	G					
YL18-2-3	R	**−0·38** ± 0·26	G					
YL18-2-4	C/R	**−0·33** ± 0·26	G					
YL18-2-5	C	**4·05** ± 0·26	D					
YL18-3-1	C	**4·03** ± 0·15	G	270	60	0·53 ± 0·02	4207	6514
YL18-3-2	C	**3·93** ± 0·15	D			0·53 ± 0·02		
YL18-4-1	C	**4·11** ± 0·26	D	220	100	0·81 ± 0·09	298	193
YL18-4-2	R	**−0·74** ± 0·26	G			0·81 ± 0·09		
YL18-4-3	C	**3·85** ± 0·26	G			0·81 ± 0·09		
YL18-4-4	C	**4·24** ± 0·26	G			0·81 ± 0·09		
YL18-5-1	C	**3·94** ± 0·26	G	260	110	0·56 ± 0·02	9994	15129
YL18-5-2	C	**3·81** ± 0·26	G			0·56 ± 0·02		
YL18-6-1	C	**3·79** ± 0·26	L	180	80	0·50 ± 0·02	4733	5696
YL18-6-2	C	**4·10** ± 0·26	L			0·50 ± 0·02		
YL18-7-1	C	**3·49** ± 0·26	D	400	90	0·55 ± 0·01	11924	5986
YL18-7-2	C	**3·48** ± 0·26	D			0·55 ± 0·01		
YL18-8-1	C	**3·22** ± 0·26	D	97	80	0·65 ± 0·01	38804	14079
YL18-9-1	C	**3·88** ± 0·26	G	175	95	0·51 ± 0·02	5091	6659
YL18-10-1	C	**3·97** ± 0·26	L	60	55	0·52 ± 0·02	9598	13071
YL18-11-1	C	**4·06** ± 0·19	G	165	80	0·52 ± 0·01	5206	5841
YL18-11-2	C/R	**3·72** ± 0·19	G			0·52 ± 0·01		
YL18-11-2	C/R	**3·42** ± 0·19	D			0·52 ± 0·01		
YL18-12-1	C	**−1·26** ± 0·19	D	115	40			
YL18-12-2	R	**−0·64** ± 0·19	L					
YL18-13-1	C	**4·83** ± 0·19	G	250	75	2·04 ± 0·21	249	195
YL18-13-2	C	**4·27** ± 0·19	G			2·04 ± 0·21		
YL18-13-3	R	**−0·25** ± 0·19	D			2·04 ± 0·21		
YL18-13-4	C/R	**1·29** ± 0·19	G			2·04 ± 0·21		
YL18-13-5	C	**3·54** ± 0·19	D			2·04 ± 0·21		
YL18-13-6	C/R	**0·77** ± 0·19	D			2·04 ± 0·21		
YL18-13-7	C	**4·32** ± 0·19	G			2·04 ± 0·21		
YL18-13-8	R	**−1·47** ± 0·20	G					
YL18-13-9	R	**−1·56** ± 0·20	G					
YL18-13-10	R	**−1·02** ± 0·20	G					

(continued)

Table 2: Continued

Crystal/spot	Core/rim	$\delta^{18}O \pm 1SD$	CL	Length (μm)	Width (μm)	Age core (Ma)	U (ppm)	Th (ppm)
YL18-13-11	C/R	**4·89** ± 0·20	L					
YL18-14-1	C/R	**0·90** ± 0·19	G	105	85	0·71 ± 0·17		
YL18-14-2	C/R	**0·97** ± 0·19	G			0·71 ± 0·17		
YL18-14-3	C	**3·34** ± 0·19	G			0·71 ± 0·17	380	236
YL18-15-1	C	**7·47** ± 0·19	G	155	70	97·5 ± 1·8		
YL18-15-2	C	**7·64** ± 0·19	G			97·5 ± 1·8		
YL18-15-3	R	**7·16** ± 0·19	G			97·5 ± 1·8		
YL18-17-1	C	−**0·19** ± 0·26	D	230	75	0·56 ± 0·09	326	275
YL18-17-2	R	−**0·61** ± 0·26	L			0·56 ± 0·09		
YL18-17-3	C	**0·51** ± 0·26	D			0·56 ± 0·09		
YL18-18-1	C	**4·19** ± 0·19	D	90	65	0·93 ± 0·09	337	244
YL18-18-2	C	**4·68** ± 0·19	G			0·93 ± 0·09		
YL18-19-1	C	**1·80** ± 0·19	D	230	70	0·79 ± 0·12	376	100
YL18-19-2	R	−**0·92** ± 0·19	L			0·79 ± 0·12		
YL18-19-3	R	**0·68** ± 0·19	D			0·79 ± 0·12		
YL18-22-1	C	**2·11** ± 0·14	G	260	65	1·51 ± 0·47	205	177
YL18-22-2	R	**0·67** ± 0·14	L			1·51 ± 0·47		
YL18-20-1	C	**1·14** ± 0·14	G	160	45	0·67 ± 0·12	650	800
YL18-20-2	R	−**1·08** ± 0·14	L			0·67 ± 0·12		
YL18-21-1	R	−**0·56** ± 0·14	L	175	50	2·84 ± 0·21		
YL18-21-2	C	**2·34** ± 0·14	G			2·84 ± 0·21	232	146
YL18-21-3	C	−**1·71** ± 0·14	D			2·84 ± 0·21		
YL18-23-1	C	−**0·55** ± 0·26	G	100	50	0·62 ± 0·17	165	108
YL18-23-2	R	−**0·60** ± 0·20	G					
SampleYL96-16 Solfatara Plateau flow (15 crystals, 32 spots)								
YL16·1__1	C	1·73 ± 0·18	L	250	120			
YL16·1__2	R	1·60 ± 0·18	G					
YL16·4__1	C	2·73 ± 0·18	G	270	90			
YL16·4__2	R	2·61 ± 0·18	L					
YL16·2__1	C	2·76 ± 0·18	G	190	120			
YL16·2__2	C	2·86 ± 0·18	L					
YL16·8__1	C	3·03 ± 0·18	L	200	80			
YL16·8__2	R	2·56 ± 0·18	L					
YL16·16__1	C	3·05 ± 0·18	G	220	80			
YL16·16__2	R	1·80 ± 0·18	L					
YL16·16__3	C	2·75 ± 0·18	G					
YL16·24__1	R	2·47 ± 0·18	L	160	80			
YL16·24__2	C	2·60 ± 0·18	G					
YL16·51__1	C	2·66 ± 0·18	D	140	60			
YL16·51__2	R	2·36 ± 0·18	L					
YL16·101__1	C	2·73 ± 0·23	L	290	130			
YL16·101__2	R	1·65 ± 0·23	G					
YL16·101__3	C	2·45 ± 0·23	G					
YL16·103__1	C	2·25 ± 0·23	L	350	170			
YL16·103__2	R	2·75 ± 0·23	L					
YL16·103__3	C	2·63 ± 0·23	G					

(continued)

Table 2: Continued

Crystal/spot	Core/rim	$\delta^{18}O \pm 1SD$	CL	Length (μm)	Width (μm)	Age core (Ma)	U (ppm)	Th (ppm)
YL16·111__1	C	2·27 ± 0·23	L	225	100			
YL16·111__2	R	2·52 ± 0·23	L					
YL16·110__1	C	2·25 ± 0·23	L	280	130			
YL16·110__2	R	2·62 ± 0·23	G					
YL16·107__1	C	2·79 ± 0·23	G	265	85			
YL16·107__2	R	2·50 ± 0·23	L					
YL16·124__1	C	3·20 ± 0·23	D	175	50			
YL16·124__2	R	2·79 ± 0·23	L					
YL16·149__1	C	2·58 ± 0·23	L	230	95			
YL16-149__2	R	1·86 ± 0·23	G					
YL16·145__1	C	2·83 ± 0·23	G	180	85			
YL16·145__2	R	2·54 ± 0·23	L					
Sample LCT-3a Lava Creek Tuff A (13 crystals 27 spots)								
LCT·2-1	C	**3·85** ± 0·15	D	120	72	0·64 ± 0·03	4279	2671
LCT·2-2	R	**2·63** ± 0·15	D			0·64 ± 0·03		
LCT·3-1	C	**3·81** ± 0·15	G	190	85	0·66 ± 0·04		
LCT·3-2	R	**3·48** ± 0·15	L			0·66 ± 0·04		
LCT·4-1	C	**3·92** ± 0·15	G	180	115	0·70 ± 0·04	2077	930
LCT·4-2	R	**4·00** ± 0·15	G			0·70 ± 0·04		
LCT·5-1	C	**4·08** ± 0·15	D	145	75	0·70 ± 0·02	4295	2811
LCT·5-2	R	**3·64** ± 0·15	G			0·70 ± 0·02		
LCT·6-1	C	**3·80** ± 0·15	L	130	70	0·62 ± 0·04	1856	1026
LCT·6-2	R	**3·72** ± 0·15	G			0·62 ± 0·04		
LCT·7-1	C	**2·91** ± 0·15	D	180	75	0·71 ± 0·03	3602	2447
LCT·7-2	R	**4·20** ± 0·15	G			0·71 ± 0·03		
LCT·8-1	C	**4·11** ± 0·14	G	163	70	0·60 ± 0·07	3679	2361
LCT·8-2	R	**3·98** ± 0·14	G			0·60 ± 0·07		
LCT·9-1	C	**4·13** ± 0·14	L	250	125	0·68 ± 0·04	1121	477
LCT·9-2	R	**4·39** ± 0·14	D			0·68 ± 0·04		
LCT·10-1	C	**3·85** ± 0·14	D	160	85	0·62 ± 0·02	3359	2015
LCT·10-2	R	**3·63** ± 0·14	L			0·62 ± 0·02		
LCT·11-1	C	**3·89** ± 0·15	G	130	70	0·66 ± 0·02	4163	2621
LCT·11-2	R	**2·97** ± 0·15	G			0·66 ± 0·02		
LCT-55-1	C	**4·31** ± 0·20	G	150	95			
LCT-55-2	R	**3·40** ± 0·20	G					
LCT-55-3	R	**2·99** ± 0·20	G					
LCT-55-4	C/R	**3·84** ± 0·20	D					
LCT-57-1	C	**4·05** ± 0·20	G	105	90			
LCT-57-2	R	**3·95** ± 0·20	L					
LCT-59-1	C	**4·16** ± 0·20	L	100	80			
LCT-59-2	R	**3·93** ± 0·20	D					
Sample BC-1 Blue Creek flow, post-HRT (14 crystals, 32 spots)								
BC1·1-1	C	**0·29** ± 0·29	D	155	85	1·80 ± 0·20	2141	1410
BC1·1-2	R	**1·81** ± 0·29	L			1·80 ± 0·20		
BC1·1-3	C	**−0·34** ± 0·29	d			1·80 ± 0·20		
BC1·2-1	C	**1·54** ± 0·29	G	170	85	2·91 ± 0·81	766	793

(continued)

Table 2: Continued

Crystal/spot	Core/rim	$\delta^{18}O \pm 1SD$	CL	Length (μm)	Width (μm)	Age core (Ma)	U (ppm)	Th (ppm)
BC1-2-2	R	**−0·55** ± 0·29	L			2·91 ± 0·81		
BC1-2-3	R	**0·82** ± 0·29	G			2·91 ± 0·81		
BC1-3-1	C	**1·55** ± 0·29	G	195	115	2·44 ± 0·66	258	167
BC1-3-2	C/R	**0·97** ± 0·29	L			2·44 ± 0·66		
BC1-3-3	R	**1·69** ± 0·29	L			2·44 ± 0·66		
BC1-4-1	C	**1·53** ± 0·29	G	115	60	2·09 ± 0·19	426	351
BC1-4-2	R	**1·74** ± 0·29	D			2·09 ± 0·19		
BC1-5-1	R	**1·57** ± 0·29	G	105	60	1·84 ± 0·19		
BC1-5-2	C	**1·30** ± 0·29	L			1·84 ± 0·19	375	263
BC1-5-3	R	**0·58** ± 0·29	G			1·84 ± 0·19		
BC1-7-1	C	**2·23** ± 0·26	D	155	60	2·14 ± 0·12	1044	802
BC1-7-2	R	**1·45** ± 0·26	L			2·14 ± 0·12		
BC1-8-1	C	**2·52** ± 0·26	D	200	60	2·03 ± 0·11	1280	1254
BC1-8-2	R	**2·28** ± 0·26	L			2·03 ± 0·11		
BC1-9-1	C	**1·59** ± 0·26	G	200	105	2·31 ± 0·3	123	68
BC1-9-2	R	**1·14** ± 0·26	G			2·31 ± 0·3		
BC1-10-1	C	**4·26** ± 0·29	G	150	125	3·22 ± 1·06	470	204
BC1-10-2	R	**5·00** ± 0·29	L			3·22 ± 1·06		
BC1-11-1	C	**4·70** ± 0·29	L	110	60	64·0 ± 1·0	280	58
BC1-11-2	R	**4·49** ± 0·29	D			64·0 ± 1·0		
BC1-12-1	C	**5·53** ± 0·29	L	115	70	2·0 ± 0·29	205	84
BC1-12-2	R	**5·41** ± 0·29	G			2·0 ± 0·29		
BC1-13-1	C	**1·19** ± 0·29	G	150	50	1·90 ± 0·15	306	208
BC1-13-2	R	**1·59** ± 0·29	L			1·90 ± 0·15		
BC1-14-1	C	**1·28** ± 0·29	G	160	85			
BC1-14-2	C	**0·98** ± 0·29	L					
BC1-14-3	R	**1·56** ± 0·29	L					
BC1-15-1	C	**0·21** ± 0·29	D	180	50	2·07 ± 0·13	451	377
BC1-15-2	R	**2·07** ± 0·29	L			2·07 ± 0·13		
Sample MFT-1 Mesa Falls Tuff (13 crystals, 17 spots)								
MFT1-12-1	C	**3·48** ± 0·26	L	115	55			
MFT1-12-2	C	**3·23** ± 0·26	D					
MFT1-12-3	R	**3·63** ± 0·26	L					
MFT1-14-1	C	**3·41** ± 0·26	D	45	35	1·45 ± 0·03	5467	4126
MFT1-16-1	C	**3·47** ± 0·26	D	62	50	1·49 ± 0·05	5305	4674
MFT1-16-2	R	**3·31** ± 0·26	L			1·49 ± 0·05		
MFT1-51-1	C	**3·55** ± 0·26	G	400	95			
MFT1-51-2	R	**3·75** ± 0·26	G					
MFT1-65-1	C	**3·70** ± 0·26	D	195	90			
MFT1-65-2	R	**3·48** ± 0·26	G					
MFT-66-1	R	**3·17** ± 0·16	G	200	90			
MFT-67-1	R	**3·60** ± 0·16	G	110	60			
MFT-68-1	C	**1·38** ± 0·16	L	50	25			
MFT-69-1	C	**3·92** ± 0·16	D	25	20			
MFT-70-1	C	**3·74** ± 0·16	G	20	20			
MFT-71-1	C	**3·67** ± 0·16	L	70	30			

(continued)

Table 2: Continued

Crystal/spot	Core/rim	$\delta^{18}O \pm 1SD$	CL	Length (μm)	Width (μm)	Age core (Ma)	U (ppm)	Th (ppm)
MFT-72-1	R	**3·28** ± 0·16	G	100	45			
MFT-73-1	C	**3·68** ± 0·16	G	110	50			
Sample YL96-9 Scaup Lake flow, post-LCT (7 crystals, 14 spots)								
YL9-1-1	C	**0·68** ± 0·16	D	390	145			
YL9-1-2	R	**2·48** ± 0·16	L					
YL9-2-1	C	**0·08** ± 0·16	G	340	140			
YL9-2-3	R	**1·81** ± 0·16	G					
YL9-3-1	C	**1·02** ± 0·16	G	340	150			
YL9-3-2	R	**2·39** ± 0·16	G					
YL9-4-1	C	**0·22** ± 0·16	G	220	110			
YL9-4-2	R	**2·24** ± 0·16	G					
YL9-5-1	C	**−0·52** ± 0·14	L	120	55			
YL9-5-2	R	**0·46** ± 0·14	L					
YL9-6-1	C	**0·68** ± 0·14	D	250	120			
YL9-6-2	R	**2·23** ± 0·14	L					
YL9-7-1	C/R	**1·98** ± 0·14	D	165	50			
YL9-7-2	R	**1·54** ± 0·14	G					
Sample HRT-2 Huckleberry Ridge Tuff Member B(10 crystals, 16 spots)								
HRTB__1-1	C	**5·33** ± 0·18	L	390	110	2·46 ± 0·10		
HRTB__1-2	R	**5·25** ± 0·18	G			2·46 ± 0·10		
HRTB__2-1	C	**5·49** ± 0·18	G	200	80	2·06 ± 0·25		
HRTB__3-1	C	**4·21** ± 0·18	D	100	95			
HRTB__3-2	R	**5·40** ± 0·18	G					
HRTB__3-3	C	**4·82** ± 0·18	D					
HRTB__5-1	C	**5·29** ± 0·18	D	150	55	2·25 ± 0·17		
HRTB__7-1	C	**5·10** ± 0·18	D	120	55	2·06 ± 0·14		
HRTB__9-1	C	**4·25** ± 0·18	D	150	95	2·34 ± 0·52		
HRTB__9-2	R	**4·70** ± 0·18	L			2·34 ± 0·52		
HRTB__11-1	C	**4·84** ± 0·18	G	420	110	1·81 ± 0·18		
HRTB__11-2	R	**5·13** ± 0·18	G			1·81 ± 0·18		
HRTB__13-1	C	**4·43** ± 0·18	G	110	65			
HRTB__13-2	C	**2·72** ± 0·18	G					
HRTB__14-1	C	**5·32** ± 0·18	G	120	110			
HRTB__16-1	C	**5·07** ± 0·18	L	60	50			
Sample HRT-C Hucklelberry Ridge Tuff Member C(12 crystals, 18 spots)								
HRTC__1-1	C	**5·15** ± 0·21	D	145	60			
HRTC__1-2	R	**5·04** ± 0·21	G					
HRTC__2-1	C	**5·60** ± 0·21	G	90	60			
HRTC__3-1	C	**4·29** ± 0·21	G	120	65			
HRTC__3-2	C/R	**3·77** ± 0·21	G					
HRTC__4-1	C	**5·45** ± 0·21	G	60	35			
HRTC__5-1	C	**5·22** ± 0·21	D	50	45			
HRTC__5-2	R	**4·69** ± 0·21	L					
HRTC__6-1	C	**4·82** ± 0·21	D	120	70			
HRTC__6-2	R	**5·63** ± 0·21	L					

(continued)

Table 2: Continued

Crystal/spot	Core/rim	$\delta^{18}O \pm 1SD$	CL	Length (μm)	Width (μm)	Age core (Ma)	U (ppm)	Th (ppm)
HRTC__7-1	C	**4·14** ± 0·21	L	130	75			
HRTC__7-2	R	**4·72** ± 0·21	G					
HRTC__10-1	C	**5·72** ± 0·21	G	150	80			
HRTC-11-1	C	**5·25** ± 0·18	D	110	50			
HRTC-11-2	R	**5·38** ± 0·18	G					
HRTC-12c	C	**4·90** ± 0·18	G	70	40			
HRTC-13-1	C	**5·66** ± 0·18	G	150	80			
HRTC-13-2	R	**5·65** ± 0·18	L					
HRTC__15-1	C	**5·94** ± 0·21	G					
Quartz analyses, Sample YL96-20 Middle Biscuit Basin flow								
QZ YL20-6-1c		**1·72** ± 0·19	**1·61**	**0·11**	**3**			
QZ YL20-6-2r		**1·49** ± 0·19						
QZ YL20-6-3r		**1·61** ± 0·19						
QZ YL20-2-1c		**2·97** ± 0·19	**1·50**	**0·75021**	**6**			
QZ YL20-2-2r		**1·61** ± 0·19						
QZ YL20-2-3		**1·13** ± 0·19						
QZ YL20-2-4		**1·06** ± 0·19						
QZ YL20-2-5		**1·08** ± 0·19						
QZ YL20-2-6		**1·13** ± 0·19						
QZ YL20-3-1		**1·40** ± 0·19	**1·27**	**0·18**	**2**			
QZ YL20-3-2		**1·14** ± 0·19						
QZ YL20-5-1		**1·23** ± 0·19						
QZ YL20-1-1c		**1·37** ± 0·19						
Quartz analyses, Sample YL96-2 South Biscuit Basin flow								
QZ YL2-1-1c		**4·30** ± 0·19	**1·46**	**0·51**	**13**			
QZ YL2-1-2r		**4·47** ± 0·19						
QZ YL2-1-3r		**4·29** ± 0·19						
QZ YL2-1-4		**4·43** ± 0·19						
QZ YL2-1-5		**4·24** ± 0·19	**4·26**	**0·18**	**7**			
QZ YL2-1-6		**4·02** ± 0·19						
QZ YL2-1-7		**4·03** ± 0·19						
QZ YL2-2-1c		**4·08** ± 0·19						
QZ YL2-2-2r		**3·92** ± 0·19	**4·00**	**0·10677**	**2**			
QZ YL2-3-1c		**4·60** ± 0·19						
QZ YL2-3-2r		**4·23** ± 0·19	**4·44**	**0·19**	**3**			
QZ YL2-3-3c		**4·50** ± 0·19						
QZ YL2-4-1c		**4·21** ± 0·19						
QZ YL2-4-2		**4·02** ± 0·19	**4·11**	**0·13718**	**2**			
QZ YL2-5-1c		**4·48** ± 0·19						
QZ YL2-8-1c		**4·70** ± 0·19						
QZ YL2-8-2r		**4·56** ± 0·19	**4·63**	**0·09829**	**2**			
QZ YL2-16-1c		**4·18** ± 0·18						
QZ YL2-15-1c		**4·03** ± 0·18						
QZ YL2-14-1c		**3·88** ± 0·18						
QZ YL2-13-1c		**4·06** ± 0·18						

(continued)

Table 2: Continued

Crystal/spot	Core/rim	$\delta^{18}O \pm 1SD$	CL	Length (μm)	Width (μm)	Age core (Ma)	U (ppm)	Th (ppm)
QZ YL2-12-1c		**3·88** ± 0·18						
QZ YL2-10-1c		**4·29** ± 0·18						
QZ YL2-9-1c		**4·87** ± 0·18						
QZ YL2-11c		**4·48** ± 0·18						
Quartz analyses, Sample LCT3a, Lava Creek Tuff								
QZ LCT-1-1		**4·46** ± 0·19	**4·27**	**0·27**	**24**			
QZ LCT-1-2		**7·66** ± 0·19						
QZ LCT-1-3		**7·83** ± 0·19						
QZ LCT-1-4		**7·36** ± 0·19						
QZ LCT-1-5		**7·70** ± 0·19	**7·06**	**1·17**	**7**			
QZ LCT-1-6		**7·12** ± 0·19						
QZ LCT-1-7		**7·27** ± 0·19						
QZ LCT-6-1		**6·76** ± 0·18						
QZ LCT-6-2		**6·65** ± 0·18	**6·70**	**0·08**	**2**			
QZ LCT-7-1		**6·35** ± 0·18						
QZ LCT-8-1		**6·51** ± 0·18						
QZ LCT-5-1		**7·15** ± 0·18						
QZ LCT-5-2		**6·74** ± 0·18	**6·94**	**0·29345**	**2**			
QZ LCT-9-1		**6·91** ± 0·18						
QZ LCT-4-1		**6·65** ± 0·18						
QZ LCT-3-1		**6·82** ± 0·18						
QZ LCT-2-1		**7·49** ± 0·18						
QZ LCT-2-2		**7·27** ± 0·18						
QZ LCT-2-3		**7·61** ± 0·18						
QZ LCT-2-4		**7·54** ± 0·18	**7·48**	**0·15**	**4**			
			6·99	**0·73847**	**19**			

CL, cathodoluminesence; D, dark; L, light; G, gray.

The intensity of ^{16}O was $\sim 2 \times 10^9$ c.p.s. ($\sim 10^9$ c.p.s./nA). The mass resolving power was set to ~2500, enough to separate hydrid interferences on ^{18}O. Two multi-collector Faraday Cups (FC) were used to measure ^{16}O and ^{18}O simultaneously, equipped with different amplifiers (10^{10} and 10^{11} Ω resistors, respectively). The base-line of the Faraday cup amplifiers was calibrated once each day; drift during the day was insignificant compared with the noise level of the detectors (≤1000 c.p.s. for one with 10^{11} Ω resistor). At each analysis position, we apply manual stage height correction (Z-focus) and automatic centering of the secondary ion before the isotopic measurement started. The internal precision of the $^{18}O/^{16}O$ ratio in a single analysis (20 cycles of 4 s integrations) yielded better than 0·15‰ (1 SE). Total analytical time per spot was about 4 min, including time for locating and selecting the analytical positions (1–2 min), pre-sputtering (10 s), automatic centering of the secondary ions (~60 s), and analysis (80 s). Data were corrected for instrumental mass fractionation (IMF) using the KIM-5 zircon standard and UWQ-1 quartz standard in the same mounts as running standards. These standards were measured four times every 10–20 sample analyses and the average value for IMF of the eight bracketing standard analyses (before and after each block of the unknowns) were used for the IMF correction. A total of 146 zircon standards and 23 quartz standards were analyzed during all analytical sessions. The external errors of eight or more standard analyses within each block of data were typically better than 0·2‰ (1 SD), which represents the spot-to-spot precision. The range of 1 SD values (see the Electronic Appendix, which is available for downloading at http://www.petrology.oxfordjournals.org) is 0·14–0·29‰, with an average of 0·19‰.

RESULTS

Table 1 provides a summary of the eruptive history at Yellowstone, the volcanic units, their ages and volumes.

We studied representative samples of each major cycle of volcanism with an emphasis on the youngest post-LCT products. Below, we provide a sample-to-sample description of the results arranged by the magnitude of the oxygen isotope heterogeneity, post-LCT magmas first, post-HRT unit next, followed by the major caldera-forming tuffs.

Zircons in post-caldera lavas

Analyses of $\delta^{18}O$ were made directly below earlier SHRIMP analysis spots to allow direct correlation of $\delta^{18}O$ and age (Fig. 2b). The highly variable values of $\delta^{18}O$ demonstrate important complexity for each sample. These results are compared with bulk analyses of many crystals using laser fluorination (Fig. 2a) for each unit. Data are plotted in Figs 3 and 4 for samples YL20, YL4, YL18, YL9, YL2, YL16, and BC1, and in Fig. 5 for LCT, MFT, and HRT [see Bindeman *et al.* (2001, appendix); crystal and sample names remain the same]. As expected, the older, pre-caldera zircon cores that are abundantly present in these samples are also higher in $\delta^{18}O$ (3–5‰), reflecting the $\delta^{18}O$ values of the pre-LCT volcanic units. However, a new result of the present work is discovery of low-$\delta^{18}O$ zircon cores surrounded by higher-$\delta^{18}O$ equilibrium rims.

Upper Basin, post-LCT, 0·5 Ma lavas

Middle Biscuit Basin, Canyon, and Dunraven Road flows (samples YL20, YL18, and YL4)

These post-LCT, 0·48–0·52 Ma, low-$\delta^{18}O$ lavas from the Upper Basin (UB) contain zircons with cores that span the preceding Yellowstone history and range from the $\delta^{18}O$ value in equilibrium with melt (−1 to +1‰) to the typical pre-LCT $\delta^{18}O$ values around +4‰ (Bindeman & Valley, 2001). An important finding of the present work is that many cores that were earlier determined to be nearly identical in their crystallization age to the 0·48–0·52 Ma Ar–Ar eruption age of their host lava in fact have $\delta^{18}O$ values that are significantly different from (higher than) the low-$\delta^{18}O$ value in equilibrium with glass of the eruption-age rim. In particular, many zircons have $\delta^{18}O$ values close to 4‰, a typical pre-caldera value. Given that such young zircons are out of oxygen isotope equilibrium with their host melt and are surrounded by a low-$\delta^{18}O$ rim, this suggests that two events occurred and that the time of transition from +4‰ to −1‰ was rapid, within the analytical resolution of U–Pb dating of these zircons (±10–20 kyr). The sequence of events during this rapid transition must have included initial intrusion and crystallization of the magmas [$\delta^{18}O(WR) = 6$‰] that crystallized the young, equilibrium 4‰ zircons [$\triangle^{18}O(WR–Zrc) \sim 2{\cdot}1$‰, e.g. Valley *et al.*, 2003]; hydrothermal alteration of the these source rocks after solidification; and heating and remelting to form small pockets of new low-$\delta^{18}O$ magma with inheritance of the normal 4‰ zircons. For example, YL20 has higher-$\delta^{18}O$ zircons with ages of

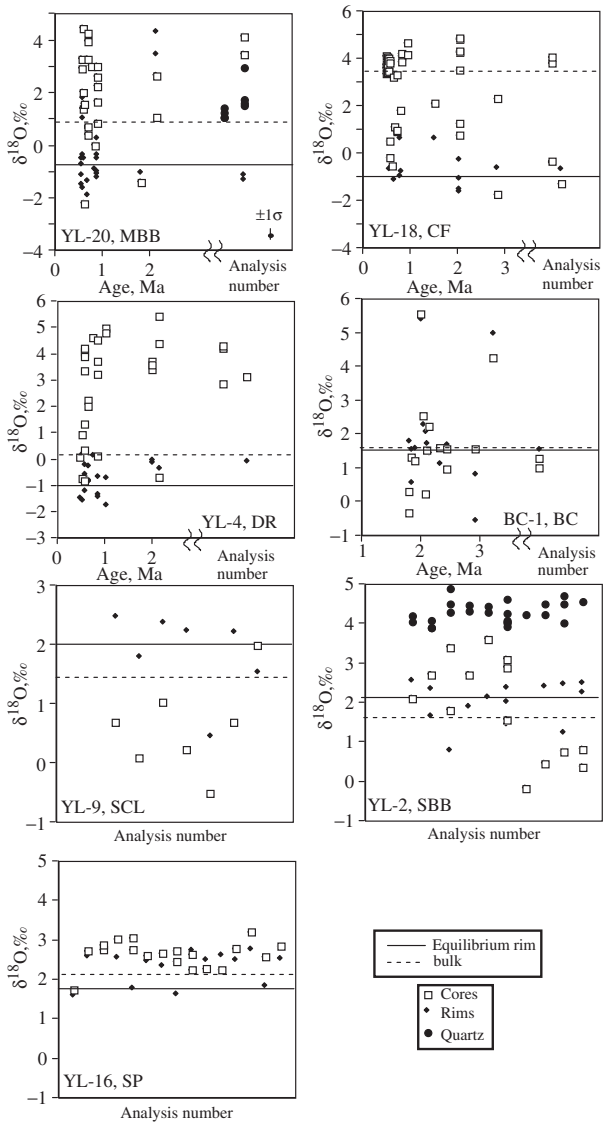

Fig. 3. Oxygen isotope ratios of zircons measured by ion microprobe in post-caldera lava units in Yellowstone plotted vs U–Pb crystallization age of the cores determined by SHRIMP (where ages are available) and undated zircons, plotted against analysis number. (See Table 2 for $\delta^{18}O$ data, zircon sizes and cathodoluminescence characteristics.) Rim values of $\delta^{18}O(Zrc)$ (diamonds) are plotted vertically above the corresponding cores (squares) for reference purposes, and have no age significance, as the majority are likely to be of eruption age. Quartz $\delta^{18}O$ values are plotted with zircons for better visualization. The continuous line represents the zircon rim value calculated to be in equilibrium with the host glass using $\triangle^{18}O(glass–Zrc) = 1{\cdot}8$‰ (Bindeman & Valley, 2002). For BC1, no fresh obsidian was available and sanidine $\delta^{18}O$ values were used ($\triangle^{18}O(glass–San) \sim 0$‰). The $\delta^{18}O$ values from laser fluorination analyses of bulk samples of zircon are shown by the dashed horizontal lines. Ion microprobe analyses of quartz (•; see Table 2) are shown for a few samples.

~0·58 Ma in their cores (0·58 ± 0·02 Ma, 0·61 ± 0·02 Ma, 0·62 ± 0·06, 0·53 ± 0·07 Ma) whereas the eruption age for this lava is 0·516 ± 0·007 Ma. Sample YL18 has $\delta^{18}O$ = 4‰ zircon cores with ages of 0·53 ± 0·02 Ma. The 0·48 Ma

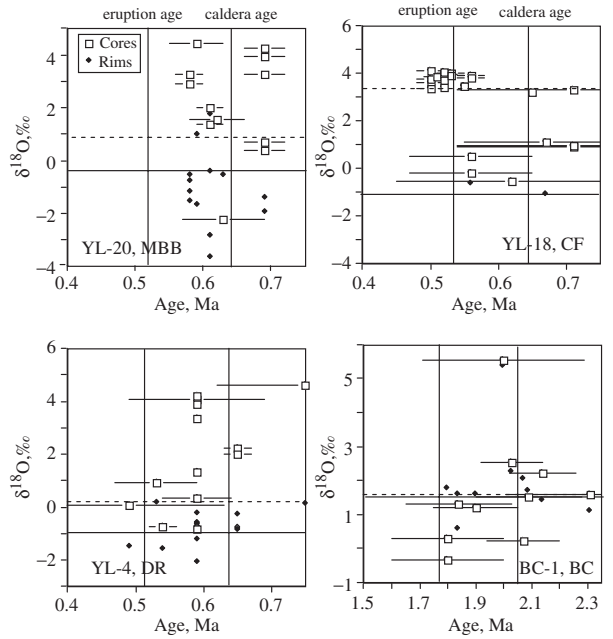

Fig. 4. Higher age resolution plot for zircons in four post-caldera samples showing the presence of high-$\delta^{18}O$ zircon cores of post-caldera age measured by ion microprobe. In each box, the left vertical line represents the Ar–Ar eruption age of these lava and the right vertical line represents the age of Yellowstone caldera collapse (0·64 Ma) for post-LCT lavas (YL20, 4, and 18), and the age of HRT caldera collapse (2·04 Ma) for post-HRT sample BC1. Horizontal error bars are 2σ age uncertainty on single analyses. (See text for discussion.)

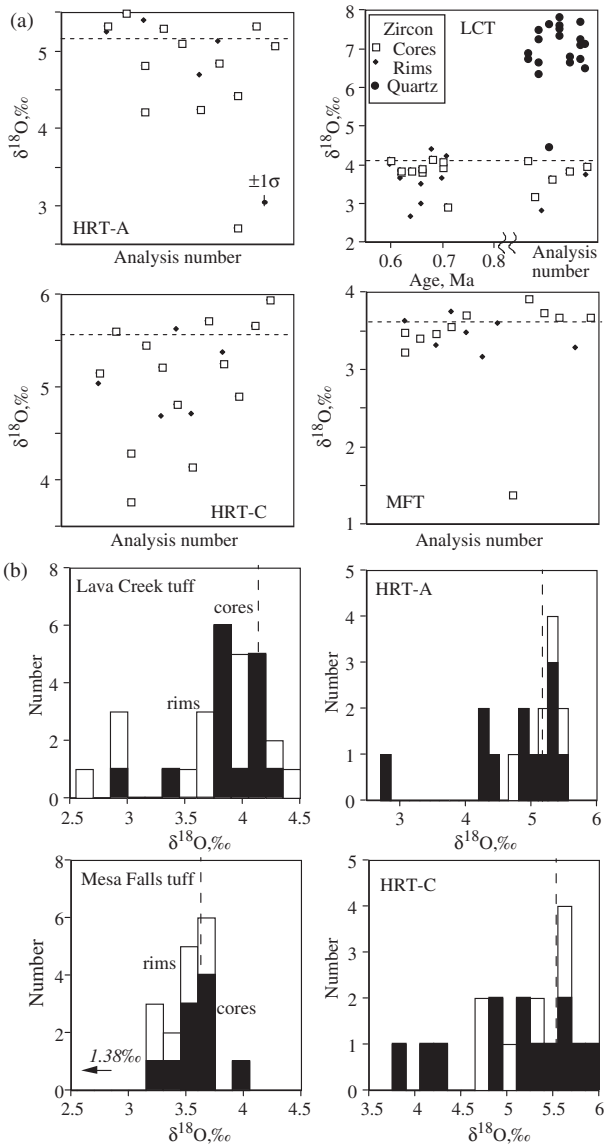

Fig. 5. Oxygen isotope ratios of zircons measured by ion microprobe in the major tuff units of Yellowstone. Ion microprobe analyses of quartz show limited intra-crystalline zoning but larger variability between crystals. Vertical or horizontal dashed lines represent average bulk analysis by laser fluorination. (a) Single analyses; zircon $\delta^{18}O$ values are plotted vs age, where $\delta^{18}O$ analyses were made directly above U–Pb SHRIMP pits; in undated zircons, the $\delta^{18}O$ values are simply plotted vs analysis number. (b) Histograms of core and rim $\delta^{18}O$ values for major tuff units.

Dunraven Road flow, sample YL4, that erupted on top of the Canyon flow sample YL18, within analytical resolution of Ar–Ar dating, contains zircon cores near its eruption age with $\delta^{18}O$(Zrc core) values of 4–0‰. It should be noted that, based on their U–Pb crystallization age, these zircon cores are post-caldera; that is, they are younger than the 0·64 Ma age of the LCT caldera formation and are distinctly younger than zircons in the LCT, the latter age clustering around 0·66 ± 0·04 Ma (Fig. 5). Below, we consider implications that these post-caldera zircons came from unerupted sub-volcanic magma batches.

Central Plateau, post-LCT, 0·25–0·1 Ma lavas

South Biscuit Basin and Scaup Lake flows (samples YL2 and YL9)

The 0·2 Ma Scaup Lake flow postdates the ~0·5 Ma low-$\delta^{18}O$ units of MBB, DR, and CF by ~300 kyr. The Ar–Ar age of SBB is determined by us to be 0·255 ± 0·011 Ma (New Mexico Tech data on sanidines, new result of the present study). These two units represent the first erupted lavas of the Central Plateau lava series that most recently erupted from 0·25 to 0·07 Ma. In these units, the new ion microprobe data establish the presence of reverse oxygen isotopic zoning relative to what we have previously found at Yellowstone: the low-$\delta^{18}O$ zircon cores are surrounded by higher-$\delta^{18}O$ rims that are in equilibrium with the host glass. This result was hinted at by our earlier bulk analyses of size fractions and abraded cores of zircons in these samples by laser fluorination (Bindeman & Valley, 2001). The $\delta^{8}O$ values of the cores of these zircons range from −1‰ to +1‰ and match the $\delta^{18}O$ of 0·5 Ma zircons contained by and in equilibrium with earlier erupted volcanic units at the same locality. Such low-$\delta^{18}O$ zircons are otherwise rare. It is, therefore, apparent that these

zircons were inherited from post-LCT, low-$\delta^{18}O$ units such as the MBB, CF, DR and their coeval subvolcanic and plutonic equivalents. It appears that the SBB lava inherited and recycled both post-LCT low-$\delta^{18}O$ and older high-$\delta^{18}O$ units, as it has cores to zircons that are both higher and lower than the value in equilibrium with the host SBB glass. It should be noted that this unit is now assigned to the Central Plateau series and exhibits strong isotopic zoning, previously unrecognized in these younger lavas.

Solfatara Plateau flow (sample YL16)

This voluminous 0·1 Ma unit is representative of one of the youngest Central Plateau Member lavas of the intracaldera volcanism. Zircons are least zoned with average bulk $\delta^{18}O$ values determined by laser fluorination of 2·05‰, plotting just below the values obtained by ion microprobe analysis (Fig. 3). It appears that the Solfatara Plateau magma marks new crystallization and/or solution reprecipitation of the previously inherited high- and low-$\delta^{18}O$ zircon cores that are seen in preceding magma batches that erupted in this part of the Yellowstone caldera (e.g. LCT, YL18 and YL4). It should be noted that a few inherited zircons were found by dating of this unit by Vazquez & Reid (2002). However, the majority of analyzed zircons have a $\delta^{18}O$ value that is ~1‰ higher than indicated for zircon in equilibrium with coexisting obsidian and quartz, and the values of $\triangle^{18}O$(Qz–Zrc) and $\triangle^{18}O$(glass–Zrc) are the smallest yet measured for Yellowstone. Selected analyses of thin zircon rims are in equilibrium with the magma, further documenting new zircon growth and the evolution towards equilibrium. This suggests that the episode of subtle $\delta^{18}O$ bulk magma depletion occurred relatively shortly before the eruption.

Post-HRT, 1·8 Ma lava

Blue Creek flow (sample BC1)

In this post-Huckleberry Ridge Tuff (HRT) unit, many zircons significantly pre-date the K–Ar eruption age of 1·75–1·78 Ma of the unit, and the age of the HRT caldera formation at 2·04 Ma, with zircon ages of 3·2–1·8 Ma. Likewise, similar to the post-LCT, there are also zircons that postdate the age of caldera formation and pre-date the eruption age within the uncertainty of the age determination of ±0·2 Ma. The $\delta^{18}O$ of zircon cores in this lava vary by 6‰. There are distinct zircons with HRT age and primitive $\delta^{18}O$ values of 5‰ surrounded by +1·5‰ rims that are in equilibrium with the glass; there are also pre-eruption age, $\delta^{18}O = 0$‰ zircon cores that are lower in $\delta^{18}O$ than the value in equilibrium with the $\delta^{18}O = 1·5$ glass. The presence of both high- and low-$\delta^{18}O$ cores in this lava is similar to the post-LCT SBB lava and suggests that multiple-source rocks with different values of $\delta^{18}O$ existed following collapse of the first caldera (HRT) and were available for remelting and inheritance during formation of the Blue Creek flow magma.

Major tuff units: LCT, MFT, and HRT

These major tuff units exhibit complexity of $\delta^{18}O$(Zrc) values that provides new information on the genesis of the parental magmas, suggesting that they were accreted from smaller magma batches with heterogeneous $\delta^{18}O$ zircon populations. These core and rim $\delta^{18}O$ values, in dated and undated zircons, can be compared with the pre-caldera values, values in equilibrium with the glass, and zircon bulk analysis by laser fluorination (Fig. 5).

Lava Creek Tuff

Zircons in the LCT have an average $\delta^{18}O$ value of $3·8 \pm 0·44$‰ (1 SD, $n = 27$) that is within analytical uncertainty of the bulk analysis by laser fluorination (4·2‰). These results suggest a lack of or limited $\delta^{18}O$ zoning; only one 0·71 Ma zircon exhibits a lower-$\delta^{18}O$ (2·9‰) core surrounded by an equilibrium (4‰) rim.

Mesa Falls Tuff

Zircons in the MFT exhibit no zoning and on average have $\delta^{18}O = 3·4 \pm 0·5$‰ (1 SD, $n = 17$), within error of the 3·6‰ bulk $\delta^{18}O$ value determined by laser fluorination. We note that this value is in oxygen isotopic equilibrium with quartz, and thus the Mesa Falls Tuff represents a large-volume (300 km^3), homogeneous, low-$\delta^{18}O$ magma. However, one zircon analysed from the MFT has a core with a significantly lower $\delta^{18}O$ of 1·38‰.

Huckleberry Ridge Tuff

Zircons in the HRT (units B and C) are the most variable among the major tuffs and cannot be treated as a single population with respect to $\delta^{18}O$. On the contrary, they represent a mixed population of zircons derived from different sources spanning more than 2‰. The bulk zircon analysis by laser fluorination yields $\delta^{18}O = 5·6$‰, which is higher than the value for many zircons measured by ion microprobe. This value best represents the average bulk $\delta^{18}O$ for all zircons in the HRT, whereas the ion microprobe data relate to specific domains imaged by CL. Both samples HRTB and HRTC contain a subset of low-$\delta^{18}O$ zircons ranging from 4·3‰ to 2·7‰. The source rocks for these low-$\delta^{18}O$ zircons could be the neighbouring Heise volcanic field in Idaho (Morgan and McIntosh, 2005) that contain abundant low-$\delta^{18}O$ magmas and zircons (Bindeman *et al.*, 2007).

Zircon overgrowths, CL intensity, and $\delta^{18}O$ profiles

Zircon rim analyses of $\delta^{18}O$ in all rocks range between the $\delta^{18}O$ of cores and the $\delta^{18}O$ of high-temperature equilibrium with the host obsidian (Figs 3–5). Multiple spot analyses were performed on dated zircons from several samples (Fig. 6). CL images were used to target the

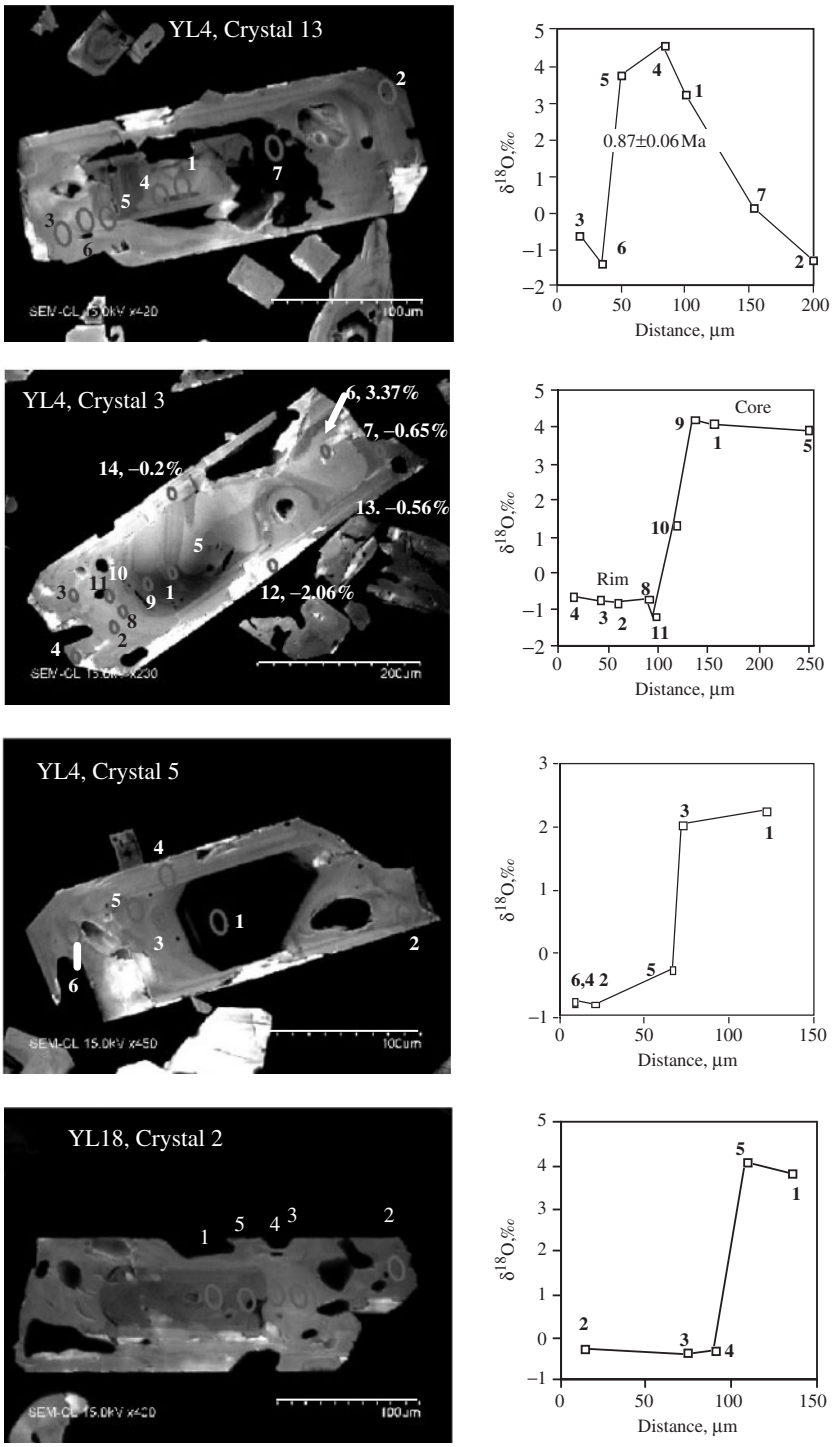

Fig. 6. Cathodoluminescence imaging of selected large zircon crystals with indicated U–Pb ages and $\delta^{18}O$ analyses by ion microprobe (from Table 2). Profiles are plotted vs distance to the zircon grain boundary. It should be noted that zircon CL zones are sharp and each zone often corresponds to distinct age and $\delta^{18}O$ values. These relations suggest episode(s) of solution–reprecipitation when zircons of different $\delta^{18}O$ value were precipitated at different times. It should be noted that three main CL zones (dark outer core, gray inner core, and rim) are seen on crystal YL4-3. Outer core values are near 4‰ despite their different age, whereas the light-CL rim value is −1, in $\delta^{18}O$ equilibrium with the glass, and its U–Pb age overlaps with the Ar–Ar eruption age of the lava.

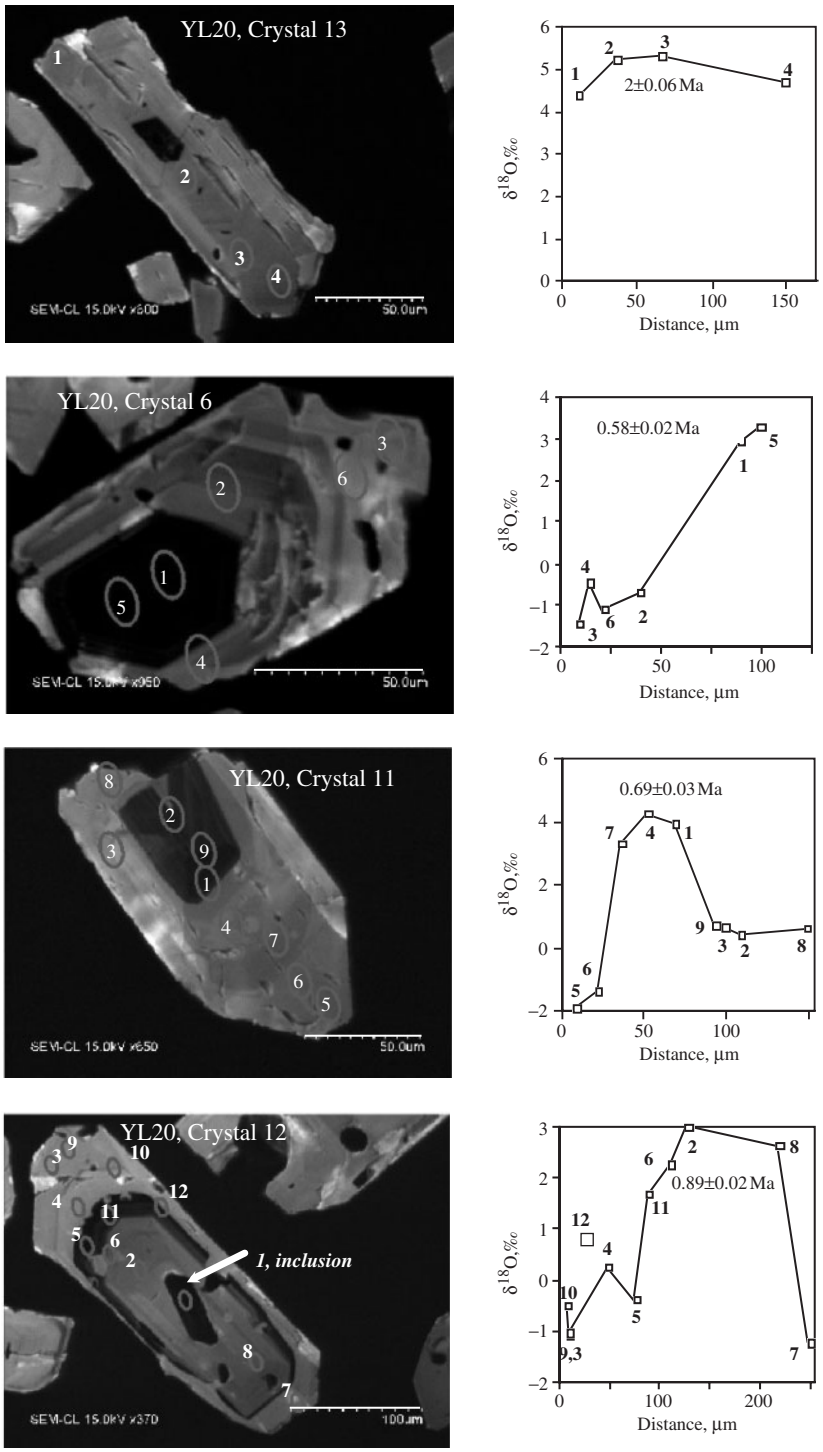

Fig. 6. Continued.

analyses, and the distance of the analysis spots from the crystal edge is given on profiles across the analyzed crystals in micrometers. The majority of crystals exhibit steep, step-like profiles with gradients of 5‰ over distances less than 15 μm between the core and the rim. Somewhat smoother profiles are observed in some crystals (6, 11, and 12) within one sample (YL20). In most cases, the CL pattern and core vs rim boundary coincide with the contrasting $\delta^{18}O$ values.

Overall, the correlation of $\delta^{18}O$ values measured by ion microprobe in zircons relative to their CL intensity

(Table 2) provides a test of the mechanism of formation for the measured gradients in $\delta^{18}O$. The CL images illustrate that light-CL zircon rims surround dark-CL cores, suggesting that the rims have lower trace element concentrations than the cores. The sharpness of most $\delta^{18}O$ profiles vs distance (Fig. 6) is too steep for them to have formed exclusively by oxygen diffusion in zircon and thus suggests that processes of zircon dissolution were followed by overgrowths of variable thickness that blanketed the core. The relatively few zircons that show more gradual transitions in $\delta^{18}O$ from core to rim are ambiguous and cannot be used to evaluate post-growth diffusive exchange vs compositional change of $\delta^{18}O$ in the magma during zircon growth.

Zircon CL patterns and trace element concentrations

U and Th concentrations were measured by SHRIMP during dating of the Yellowstone zircons (Bindeman *et al.*, 2001; Table 2), and by electron microprobe (Fournelle *et al.*, 2000; Bindeman & Valley, 2001) but have not been discussed previously in any detail. Here we describe the trace element compositions in the context of our new CL imaging (Fig. 6), as CL intensity is largely controlled by the trace element concentrations (Kempe *et al.*, 2000).

Trace element concentrations were analyzed with a 2–4 μm^2, 400 nA electron microprobe beam by profiling and 2D mapping of U, Th, Y, and Ce (Fournelle *et al.*, 2000; Bindeman & Valley, 2001). Like the CL patterns in Fig. 6, the trace element zoning profiles vary from abrupt and complex to smooth [crystals a–e in fig. A2 of Bindeman & Valley (2001)]. We interpret the smooth variations as indicative of zoning developed during crystal growth, whereas the more complex trace element patterns resulted from sector zoning (crystal b) and abrupt variations around resorbed cores (e.g. crystals c, d, and e) provide evidence of inherited cores. On these images, dark-CL cores and dark-CL zoning patterns always correlate with high concentrations of U, Th, Y, and Ce. This correlation is well known by U–Pb ion microprobe geochronologists, who target dark-CL, high-U areas for analysis of young zircons (higher concentrations of daughter isotopes) and bright-CL zones for analysis of ancient zircons (less radiation damage and common Pb). Zircon CL intensity is determined in part by the middle REE elements, notably Dy, and by radiation damage (e.g. Kempe *et al.*, 2000).

Concentrations of U and Th in Yellowstone zircons range from 100–1000 ppm (values that are normal in other rocks) to extremely elevated values (up to 39 000 ppm U and 15 000 ppm Th). The identity of the analyzed crystals was checked to verify that they were indeed zircon and not chevkinite, a REE-rich mineral that has modest Y, U, and Th concentrations. The U and Th concentrations do not correlate with age or $\delta^{18}O$ value,

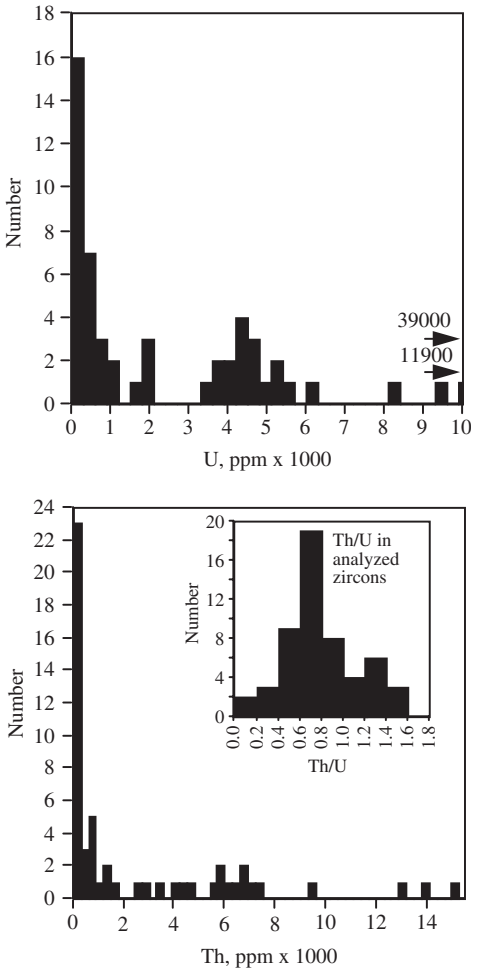

Fig. 7. The U and Th concentrations and Th/U ratios in Yellowstone zircons [data from Bindeman *et al.* (2001, appendix)]. The bimodal distribution of U concentrations should be noted; this is interpreted here as representing volcanic and plutonic zircons (see text for discussion).

and both old and young inherited zircons may be U- and Th-rich. Samples of the major tuffs have typical (HRT) to elevated (LCT) concentrations of U and Th in their zircons, but the most U- (and Th)-rich zircons (>3000 ppm) occur in post-caldera low-$\delta^{18}O$ units and in the LCT (Fig. 7). The Th/U ratio ranges from 0·2 to 1·5. Post-caldera low-$\delta^{18}O$ zircons account for most of the variability in Th/U and for the higher values, which are at the upper end of typical Th/U ratios reported elsewhere for zircons (e.g. Hoskin & Schaltegger, 2003).

Quartz $\delta^{18}O$

Phenocrysts of quartz were analyzed for $\delta^{18}O$ by ion microprobe in three samples: two post-LCT, low-$\delta^{18}O$ units (YL2, 14 crystals; YL20, five crystals) and normal-$\delta^{18}O$ LCT tuff (nine crystals) (see Table 2). All analyzed quartz crystals exhibit complex oscillatory CL zoning

patterns characteristic of igneous quartz, with distinct brighter and darker growth bands in some crystals.

The $\delta^{18}O$ values of quartz phenocrysts are close to being in isotopic equilibrium with the host obsidian ($\triangle_{Qz\text{-}rhyolite} = 0{\cdot}5‰$ at 750°C, Bindeman & Valley, 2003). Most crystals exhibited no $\delta^{18}O$ zoning. A higher-$\delta^{18}O$ core and equilibrated rim is present only in one crystal in low- $\delta^{18}O$ sample YL20. However, crystal-to-crystal variability within each sample (~1‰) is in excess of our 2 SD analytical uncertainty (±0·36‰) and therefore reflects real natural variability. Furthermore, secondary ionization mass spectrometry (SIMS) analyses can be compared with laser fluorination analyses of single quartz crystals, and size fractions of quartz crystals (Bindeman & Valley, 2001). Sample YL20 has a 0·9–1·4‰ range in $\delta^{18}O$ by laser vs 1·1–3·0‰ by ion microprobe, with a calculated equilibrium value vs glass of 1·35‰. The quartz in YL2 has a range of values from 6·2 to 4·2‰ measured by laser vs 3·9–4·9‰ by ion microprobe, and a calculated equilibrium with glass value of 4·2‰. Sample LCT has a range of 6·5–6·8‰ by laser vs 4·5–7·8‰ by ion microprobe, and a calculated equilibrium value of 6·0‰.

Exchange of oxygen isotopes by diffusion would be expected to form smooth, inflected, error function-shaped core-to-rim zoning. Such profiles in $\delta^{18}O$ are not observed in the quartz crystals analyzed by ion microprobe. Thus, processes of solution and reprecipitation seem to be more important for quartz than intracrystalline diffusion, as is seen in some CL images (e.g. Bindeman & Valley, 2001, fig. 2).

DISCUSSION

Evidence for remelting and zircon inheritance as a result of magmatic reheating

Isotopically diverse (U–Pb and $\delta^{18}O$) zircons in each sample are surrounded by a rim of variable thickness that is in equilibrium with glass (Fig. 6). In the majority of cases, cores are dark in CL, whereas rims are bright in CL. Some of these high-$\delta^{18}O$ or low-$\delta^{18}O$ cores show clear evidence of crenulated core–rim resorption boundaries; the majority show more crystallographically controlled core–rim boundaries. Occasionally, there is evidence of two concentric cores surrounded by a rim, which might indicate a maximum of two episodes of dissolution and inheritance (e.g. YL4, crystal 13, Fig. 6). These rather simple core–rim relations suggest a single dissolution–reprecipitation episode caused by a temperature increase, followed by zircon rim crystallization during cooling. Collectively (with some added complexity for single grains), the zircon population in each post-caldera sample records a single remelting episode (Bindeman & Valley, 2000).

The time gap between the youngest high-$\delta^{18}O$ core and the low-$\delta^{18}O$ rim is analytically indistinguishable by U–Pb dating (i.e. <10–20 kyr). We have presented evidence above that inheritance in low-$\delta^{18}O$ lavas included a subset of zircons of post-caldera (LCT or HRT) age (Fig. 4). These zircons suggest that a 0·1–0·15 Myr gap separates caldera collapse and the appearance of the first low-$\delta^{18}O$ post-caldera units. During this time gap, magmas with LCT- (or HRT)-like zircons, unknown on the surface as lavas, continued to intrude as dikes and sills into the collapsed intra-caldera block, which subsequently became the magma generation zone for the low-$\delta^{18}O$ magmas.

Volcanic or subvolcanic (plutonic) zircons?

The results of the present work emphasize the importance of the volcanic–plutonic connection between granitic batholiths and their coeval erupted counterparts. Zircon cores that are variable in $\delta^{18}O$, and that have diverse ages, constitute a majority in each post-caldera lava, and are present at lower concentrations in the large-volume tuff units. It is logical to suggest that these zircons were inherited from source rocks of variable age and variable-$\delta^{18}O$ values. This inheritance may be from hydrothermally altered, low-$\delta^{18}O$, volcanic rocks that were buried in the magma generation zones by successive caldera collapses, and from their coeval sub-volcanic intrusions in the intra-caldera block. Many zircons match the isotopic ratios and age of older pre-caldera surface units.

We have presented evidence above of strikingly variable trace element concentrations in Yellowstone zircons, most notably in U, Th, and the REE. Below we argue that some U- and Th-rich zircons crystallized from the last portions of incompatible element-rich melts, and thus must have been inherited from the unerupted sub-volcanic–plutonic equivalents of exposed (or unexposed) surface units. Assuming that high-U zircons reflect equilibrium crystallization from a U-rich melt, and assuming a partition coefficient $D_{zircon/melt}$ of 300 (Mahood & Hildreth, 1983) for the high-silica rhyolitic melt, zircons with 3000 ppm of U could have crystallized from a melt with 10 ppm U. The Yellowstone rhyolites contain 4–7 ppm U (Hildreth *et al.*, 1991). Fifty per cent crystallization of a 5 ppm U rhyolite involving a feldspar + quartz + accessory zircon assemblage may have doubled the U concentration in the residual melt if the amount of zircon in the cumulates was less than 1 wt%, thus yielding a cumulate/melt bulk partition coefficient of ~0·3. For comparison, Lu *et al.* (1992*a*, 1992*b*) estimated $D_U = 0{\cdot}2$ for lower-temperature Bishop Tuff rhyolites. Thus, for typical Yellowstone magmas, 50% fractional crystallization is capable of generating an ~10 ppm U melt from a crystal mush and 3000 ppm U in zircons.

Zircons with higher than 3000 ppm U could crystallize only if the melt underwent much more extreme fractionation. A simple fractional crystallization calculation with

a bulk cumulate/melt Zr partition coefficient of 0·3 requires 95% crystallization of an initial 5 ppm U rhyolite to generate a residual melt with pegmatite-like U concentrations of 41 ppm, crystallizing zircon with 12 100 ppm U. The two most extreme Yellowstone zircons (YL18-7·1 with 12 000 ppm U, and YL18-8·1 with 39 000 ppm U) would thus suggest >80 ppm U in the 'pegmatitic' parent melt, and >98% crystallization.

Similar reasoning applies to other trace elements measured in zircon. For Th and Y with typical concentration in Yellowstone rhyolites of 25 ppm and 50 ppm, respectively (Hildreth *et al.*, 1991; Bindeman & Valley, 2001), and $D_{\text{zircon/melt}} = 100$ for both (e.g. Mahood & Hildreth, 1983), the cut-off concentration in zircon is ~4000 ppm (Th) and ~8000 ppm (Y). Thus, high-Y zircons (Y >10 000 ppm; Bindeman & Valley, 2001, fig. A2e and f) must have had a plutonic (sub-volcanic) origin, and crystallized from a residual or pegmatitic melt.

We propose to use 3000 ppm U in zircon as the level that distinguishes zircons that were inherited from volcanic precursor rocks (<3000 ppm) from those inherited from sub-volcanic (plutonic) rocks. This 3000 ppm cut-off corresponds to 40–60% crystallinity, which is the rheological limit for extractability of melt from a crystal mush (e.g. Marsh, 1981), and melt extraction would be possible only through hindered settling mechanisms (e.g. Bachmann & Bergantz, 2004). Using these arguments and surveying Yellowstone zircons for grains with higher than 3000 ppm U and 4000 ppm Th using the supplementary dataset of Bindeman *et al.* (2001), 31 out of 114 zircons based on U, and 19 out of 114 zircons based on Th, represent inheritance from crystalline, 'plutonic' or sub-volcanic rocks. However, this estimate is biased toward 'plutonic' zircons because we targeted dark-CL, higher-U, grains during dating. Sub-volcanic or plutonic zircons are also common in other caldera systems (e.g. Bacon & Lowenstern, 2005; Charlier *et al.*, 2005). The observation that dark-CL cores with high U, Th, and Y contents are often surrounded by light-CL, trace element poorer rims (Fig. 6) suggests a pre-eruptive dissolution–overgrowth episode and rim crystallization from a higher-degree, trace element poorer melt.

Other phenocrysts showing inheritance

Trace and major element analyses of melt inclusions in UB lavas (MBB and CF) and the Scaup Lake flow (Gansecki, 1998; Bindeman & Valley, 2001) exhibit very diverse compositions, with higher concentrations of some incompatible elements in melt inclusions as compared with the whole-rock and groundmass values. A lack of any correlations may further support the conclusion that quartz is xenocrystic and was derived from pre-caldera rocks, which are diverse in composition and age.

Furthermore, strontium isotopic differences between plagioclase and groundmass mentioned by Gansecki (1998, p. 86), as well as xenocrystic feldspar contamination based on Ar–Ar (Gansecki *et al.*, 1996), further suggest that many of the feldspars are inherited, and resided for 5–10 kyr in the magma prior to eruption. Feldspar and zircon inheritance from pre-existing volcanic rocks was also observed in the products of the Crater Lake caldera-forming eruption (Bacon & Lowenstern, 2005).

Solution–reprecipitation, isotope zoning and variability in zircons

Bindeman & Valley (2000, 2001) suggested that two processes control the isotope exchange between quartz, zircon, and melt, both leading to the establishment of equilibrium of grain boundaries with glass: intra-crystalline diffusion of oxygen and solution–reprecipitation. The results of the present ion microprobe study of isotopically heterogeneous zircon crystals demonstrate the abundance of step-function profiles, corresponding to a solution–reprecipitation episode caused by a thermal spike. Based on textural evidence and *in situ* $\delta^{18}O$ analyses, this also suggests that dissolution and overgrowth rates are faster than the oxygen diffusion rate, or that dissolution–precipitation had overtaken diffusion at some later point, erasing evidence of past diffusion. Below, we attempt to quantify rates of solution–reprecipitation relative to the rate of diffusive isotopic exchange (Fig. 8).

The growth and dissolution rates of zircon are controlled by the rate of zirconium diffusion through the rhyolitic melt away from the growing or dissolving boundary (Harrison & Watson, 1983; Watson, 1996). Zircon dissolution and growth is a sequential process that also involves interface reaction and volume diffusion (Zhang *et al.*, 1989). Based on Fick's First Law, the diffusive flux away from the dissolving boundary is a function of the Zr gradient; that is, the rate of diffusion is a linear function of zircon undersaturation in the melt for each given dissolution zone thickness. Watson (1996) combined saturation and dissolution conditions into the single equation

$$\frac{dr}{dt} \times 10^{17} = -U \frac{1.25 \times 10^{10}}{r} \left[\exp\left(\frac{-28380}{T}\right) + 7.24 \times 10^{8} \exp\left(\frac{-23280}{T}\right) \right] \quad (1)$$

where U is the degree of undersaturation (dissolution) or oversaturation (growth) in the magma in ppm, r is the crystal radius in cm, T is the temperature in Kelvins, and the linear dissolution rate dr/dt is expressed in cm/s. It is clear that the dissolution rate is directly proportional to the degree of undersaturation. In our subsequent treatment we assume that Zr undersaturation in Yellowstone magmatic systems is large (40–80 ppm Zr), as a result of the rapid T increase. For example, 40 ppm undersaturation corresponds to ~8°C of overheating for high-silica eutectoid rhyolitic compositions using the saturation equation

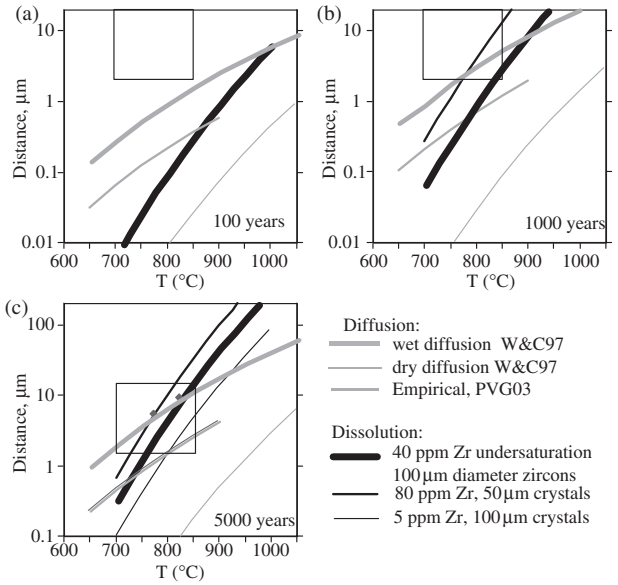

Fig. 8. Modelling the role of solution–reprecipitation and diffusion for developing zircon overgrowth and core-to-rim isotope zoning. The graphs compare diffusion and overgrowth distances that would develop over three different time periods. For dissolution–overgrowth rates, we use the 1D solubility–diffusivity equation (1) in the main text (Watson, 1996) assuming zircon undersaturation of 40, 80, and 5 ppm, and crystal diameters of 100 μm and 50 μm. Diffusion distances in zircon are calculated from the relation $x = \sqrt{Dt}$. Diffusion coefficients for diffusion of oxygen in zircon are from Watson & Cherniak (1997, wet and dry, experimental; W&C97) and Peck *et al.* [2003; PVG03; extrapolated from lower temperatures for metamorphic rocks, empirical (Page *et al.*, 2007)]. Rectangles of 1–10 μm and 700–850°C in each panel are shown for reference and correspond to characteristic distances of zircon rims and temperature estimates for Yellowstone rhyolites from Bindeman & Valley (2001). (a) Diffusion and overgrowth distances for 100 years. It should be noted that, on short timescales, diffusion overtakes dissolution rates. The diffusion distances are short (0·5–2 μm at $T = 750$–850°C) and dissolution distances are even shorter. Therefore 100 years is too short a time to explain the thickness of overgrowth rims shown in Fig. 6 even at temperatures as high as 850°C. (b) Diffusion and overgrowth distances for 1000 years. Wet diffusion of Watson & Cherniak (1997) still overtakes dissolution–overgrowth rates, except for the highest (80 ppm) Zr oversaturations and smallest (<40 μm) zircons, at higher than 775°C. If empirical estimates for D are used, which indicate slower oxygen diffusion in zircon, then zircon dissolution rates are faster. For relevant Yellowstone parameters either wet diffusion or dissolution (>775°C, >80 ppm undersaturation) is capable of generating the observed diversity of rim thicknesses. (c) Diffusion distances for 5000 years. On these relatively long timescales, dissolution at high undersaturation overtakes diffusion at the highest peak temperatures, and would have erased any diffusive boundary that developed during the progressively longer residence time and temperature increase. Subsequent zircon crystallization coupled with temperature decrease would lead to overgrowth rim thicknesses that are comparable with those observed.

of Watson & Harrison (1983). We believe that these conditions would adequately characterize intra-caldera rocks that are rapidly heated and melted in the presence of residual zircons.

Figure 8 shows linear dissolution distances in zircon for 100, 1000, and 5000 years keeping all indicated conditions constant, and compares these dissolution distances with diffusion distances of oxygen for the same time duration using published diffusion coefficients of oxygen in experimental (wet, dry), empirical, and buffered conditions (Watson & Cherniak, 1997; Peck *et al.*, 2003; Page *et al.*, 2007).

Dry diffusion conditions for oxygen in zircon are unrealistic for hydrous, ~3 wt % H_2O, Yellowstone rhyolites and dry diffusion rates in zircon would indicate negligible exchange on these timescales. If dry diffusion coefficients are applicable, then solution–reprecipitation rates dominate for all temperatures at which zircon can crystallize.

Diffusion is fairly fast initially, when the concentration gradient is the steepest. If the oxygen diffusion coefficient from hydrous experiments on zircon is used (wet diffusion), the diffusion would overtake dissolution on short, <100 year timescales regardless of the choice of diffusion coefficient (Fig. 8a). However, diffusive exchange will be limited to only 0·5–2 μm in zircon (Fig. 8a), and such short diffusion distances will not affect the $\delta^{18}O$ of the cores of zircons. Dissolution–overgrowth rates are slower and are incapable of explaining the observed pattern of isotopic zoning on timescales of 100 years or less.

On longer timescales, diffusion rates become slower than the dissolution rate at large undersaturations (kept fixed in the modeling), but the transition from diffusion-control to dissolution-control depends on the diffusion coefficient of oxygen. If wet oxygen diffusion coefficients as experimentally determined by Watson & Cherniak (1997) for $P(H_2O)$ >70 bars are employed, then it will take higher temperatures and degrees of undersaturation for solution–reprecipitation to overtake diffusion, and this will require 5000 years at temperatures appropriate for the Yellowstone rhyolites. If wet diffusion coefficients were 20 or more times lower (e.g. Peck *et al.*, 2003; Page *et al.*, 2007), then dissolution–reprecipitation will overtake diffusion earlier, after ~1000 years of residence. In these calculations significant degrees of zirconium undersaturation of >30 ppm were maintained. As a result of 5000 years of dissolution, a significant proportion of the original zircon, 1–20 μm radial, will be dissolved. Therefore, even if a micrometer-scale diffusion profile formed on zircons at an early stage, the subsequent dissolution on longer timescales will overtake this zoned boundary, leaving a step-function melt–zircon boundary at the end of the dissolving cycle. Another observation from Fig. 8 is that the role and the rate of solution–reprecipitation increases much more steeply with increasing temperature than that of diffusion, and the undersaturation parameter, U, stays large, thus enhancing the role of dissolution at higher temperature. Following heating and dissolution, zircons and their host melt will cool; a common rim will form on inherited cores with a sharp core–rim boundary. If the same rate of undercooling is kept, it would take 5000 years to crystallize

10–20 μm thick rims around zircons while preserving a step-function core–rim oxygen isotope profile, as seen at Yellowstone (Fig. 6). Two distinct rims within some zircons may indicate that heating–precipitation episodes do not always lead to an eruption. In Yellowstone and elsewhere, undercooling could occur as a result of extrusive cooling and/or as a result of hydrothermal refrigeration of melt pockets by circulating meteoric fluids.

The other approach to evaluate competition between diffusion and solution–reprecipitation is the use of the growth Peclet number, which compares the relative importance of these two processes. The growth Peclet number is defined as $Pe = VL/D$, where V is the dissolution or crystallization rate, L is the dissolution distance of the dissolving grain, and D is the diffusion coefficient of oxygen in the crystal lattice of the dissolving grain. Watson & Liang (1995) used this analysis to explain the abundance of sector zoning in zircon and sphene as a result of slow diffusion of REE (which affect CL) in these minerals and assumed a molecular layer of 5 nm to represent the characteristic length L. If the diffusion coefficient of oxygen in zircon is of the order of 10^{-18}–10^{-20} cm^2/s (see Fig. 8 for 850°C, WC97, wet) the dissolution rates of zircon need to be appreciably larger than 2×10^{-11} to 2×10^{-13} cm/s for dissolution to overtake diffusion. At these dissolution rates $Pe \gg 1$, and the solution–reprecipitation will play a more important role than diffusion.

The conclusion that solution–reprecipitation is the dominant process for zircon is also valid for quartz, which is demonstrated by ion microprobe analysis to be much more homogeneous in $\delta^{18}O$ than zircon; this is explained by faster rates of solution–reprecipitation for quartz than for zircon. This comes as no surprise, as silica solubility and diffusion in rhyolites is greater than that for zirconium (Baker, 1991).

Bindeman & Valley (2000, 2001) estimated that it took 500–5000 years to develop the oxygen isotope variability seen in size fractions of zircon and quartz from post-LCT low-$\delta^{18}O$ lavas, and ~10 000 years for the post-HRT Blue Creek flow. These estimates were based on consideration of isotope diffusion rates in quartz and in zircon of different sizes, and quartz–zircon isotope disequilibria. Elsewhere, Bindeman & Valley (2003) interpreted more annealed isotope zoning in zircons from Timber Mountain, Nevada, to represent 10 000 years of residence. These estimates would stay the same within a factor of ~2 given the arguments on timescales above.

Zircon sampling and survival upon remelting

Poly-age zircon populations found in the post-caldera Upper Basin lavas clearly suggest that they sample Yellowstone rocks ranging from the 2·1 Ma HRT to unerupted 0·6–0·5 Ma post-LCT sub-volcanic units. Zircons of similar age groups are present in post-LCT lavas erupted in the NE (CF, DR) and SW (MBB) parts of the caldera, 40 km apart (Fig. 1). It is obvious that pre- and post-caldera units are present in different parts of the caldera, and are likely to be complexly juxtaposed and intercalated within the intra-caldera block; thus geographical location may explain differences in the abundance of inherited zircons of different age.

The other reason for zircon abundance and survival is the different concentrations of Zr in the parental host-magmas, which vary by a factor of three from 170 to 550 ppm (Bindeman & Valley, 2001). Thus, even for an equivalent temperature increase in these rocks, saturation–dissolution conditions could be met for one magma composition but exceeded for another. As a result, zircons of different age will have a different probability of survival upon heating episodes of equal length. In this regard it is interesting to point out that the HRT-age (~2 Ma) zircons have a resorbed morphology and are surrounded by only a thin rim. The Huckleberry Ridge Tuff has one of the highest Zr concentrations (up to 450 ppm) of any subsequent Yellowstone magma, and thus the highest zircon saturation temperature. HRT-age zircons are present throughout the post-HRT and post-LCT units. In contrast, zircons in a host magma with a low zircon concentration, such as MFT (~160 ppm), will probably be completely dissolved, and these zircons are notably lacking among the dated zircon population (Bindeman *et al.*, 2001), despite representing one of the most voluminous rhyolites at Yellowstone. Furthermore, different zircons exhibit rims with different thickness, suggesting that they started dissolution upon capture at times that may differ by hundreds of years to a few thousand years.

Concave-downward zircon crystal size distributions reported for Yellowstone rocks by Bindeman & Valley (2001) and Bindeman (2003) are consistent with a heating episode after the beginning of zircon growth. Heating in a melt to above zircon saturation will result in the total disappearance of crystals smaller than a certain threshold diameter. Subsequent growth on the surfaces of resorbed cores and subdued new nucleation will result in a lower abundance of the smallest crystals. However, the inherited cores are texturally concealed in the final crystal size distribution.

YELLOWSTONE MAGMATISM—PROGRESSIVE SELF-CANNIBALIZATION VS MUSHY MAGMA

Vazquez & Reid (2002) advocated a single magma source derivation for the Central Plateau Member (CPM) lavas from an LCT-like crystal mush remaining in the crust, which might represent a partially solidified LCT batholith. They contrasted the 0·25–0·1 Ma CPM units with the ~0·5 Ma Upper Basin CF, MBB, and DR lavas dated by

Bindeman *et al.* (2001), and quoted the following evidence for mush derivation of the former: the CPM units are distinct from the UB lavas and have a less radiogenic Sr isotopic composition, fewer zircon xenocrysts, and seemingly similar zircon crystallization age for subsets of zircons in spatially separated voluminous lavas.

Vazquez & Reid (2002) presented chemical and $(^{87}Sr/^{86}Sr)_{whole\ rock}$ trends indicative of progressive increase in Rb/Sr ratio as a result of feldspar fractionation, followed by aging for tens of thousands to hundred of thousands of years. We note that the uncertainty of age determination based on U–Th disequilibria dating of rather old volcanic units is tens of thousands of years and thus multiple interpretations of petrogenesis within this timeframe are thermally feasible; these may be related either to independent magma batches or to a single long-lived magma mush. We have presented evidence above that post-caldera, younger than LCT, high-$\delta^{18}O$ zircons are present throughout the low-$\delta^{18}O$ post-LCT lavas (Fig. 4), and that the time required for the intrusion of their parental magma, hydrothermal alteration, and sampling by inheritance may have been less than several tens of thousands of years, well within the uncertainty of the U–Th dating.

High concentrations of Sr in Yellowstone feldspars (400–500 ppm, Doe *et al.*, 1982; Gansecki, 1998) yield high bulk feldspar–rhyolite partition coefficients D_{Sr} of 12–20, comparable with the $D_{Rb/Sr}$ values of Lu *et al.* (1992*b*) and Anderson *et al.* (2000). D_{Rb} in the bulk crystallizing assemblage is low (~0·1, Mahood & Hildreth, 1983). As a result, to change the Rb/Sr ratio from 20 to 200, which is similar to the most extreme differences between the UB magmas and the most evolved CPM magmas, fractionation of only 5% feldspar, or 7·5% of the total phenocrysts in the proportion 33% quartz, 33% sanidine, 33% plagioclase is required. Rb/Sr (and likewise Ba/Sr) ratios in whole-rocks vary by a maximum of one order of magnitude in most of the LCT, UB, and CPM magmas (Bindeman & Valley, 2001); the majority of the interstitial glasses in these units have Rb/Sr of 21·4–81·4 (Vazquez & Reid 2002), with extreme values from the Pitchstone Plateau (140) and Scaup Lake (2·76) flows.

Because we interpret UB magmas as inheriting many feldspars from their crustal source rocks, supported by differing $^{87}Sr/^{86}Sr$ ratios in these feldspars (Gansecki, 1998), variations in the Rb/Sr ratio by a factor of 10 may indicate only 7·5% addition or subtraction of phenocrysts dominated by feldspar, not the 40% assumed by Vazquez & Reid (2002). Such small proportions do not require the magmas to be a mush; 10 or 20% fractionation is easily accomplished in small magma batches via crystal settling, or separation during ascent.

Perhaps the strongest evidence for the presence of distinct magma batches, and not a single mushy magma body, comes from the distinct $\delta^{18}O$ values of the West Yellowstone, Solfatara Plateau, Scaup Lake, Pitchstone Plateau and Gibbon flows (see Fig. 2, Table 1; Hildreth *et al.*, 1984; Bindeman & Valley, 2001) and the $\delta^{18}O$ (quartz–zircon) fractionations that are specific for each unit, which require them to be separate magma batches, rather than the products of the same progressively differentiating and homogeneous magma mush.

The critical evidence for the distinct nature of at least three of the 0·25–0·1 Ma CPM lava units (SBB, SCL, SP) comes from the $\delta^{18}O$ values of single zircons (Fig. 3), which show that nearly the entire population of these zircon cores is inherited. Furthermore, they also contain a variable population of low-$\delta^{18}O$ zircon cores that were inherited from the 0·5 Ma UB post-LCT lavas. We suggest that the voluminous lavas that erupted at Yellowstone between 0·25 and 0·1 Ma trace the same path of evolution as the 0·5 Ma UB lavas. Thus, each lava represents an independent parcel of melt generated and erupted independently by nearly complete remelting of hydrothermally altered high-silica rhyolitic protoliths that had open fractures and were probably below their solidi prior to melting.

However, these interpretations, and the conclusions of Vazquez & Reid (2002) are not mutually exclusive. Coexisting pockets of melt that differentiate feldspars to develop variably high Rb/Sr correlations may cool to below the solidus induced by neighboring hydrothermal circulation and become hydrothermally altered for tens of thousands of years. In such a model, the hydrothermal fluids not only alter the groundmass of these rocks but also serve as an effective refrigerant. This interpretation would suggest that differentiating pools of magma and hydrothermal cells coexist side by side.

Magma isotopic 'recovery' after caldera collapse

Increases and decreases in Sr and Pb isotopic ratios are seen during the evolution of the Yellowstone magmatic system, with $^{87}Sr/^{86}Sr_i$ increasing from 0·711 to 0·719, and $^{206}Pb/^{204}Pb$ increasing from 17·4 to 17·9 from the LCT to the low-$\delta^{18}O$ UB lavas. Hildreth *et al.* (1984, 1991) interpreted these increases as evidence for a high-$^{87}Sr/^{86}Sr_i$, high radiogenic lead, but low-$\delta^{18}O$, meteoric water-derived brine mixing with the LCT magma after caldera collapses. Furthermore, recovery of these isotopic ratios towards more LCT-like values in the subsequent CPM lavas was interpreted as an indication of magma mixing between contaminated UB-type magma and the remaining large volume of LCT-type magma.

Caldera collapse is a dramatic event in the history of any magmatic system and compositional and isotopic changes are expected as the rule, rather than the exception. Geologically, the UB lavas postdate the resurgent rise of the Mallard Lake and Sour Creek domes. The connection between the timing and mechanisms

of resurgent doming and UB lavas needs to be investigated further. Improved Ar–Ar dating (e.g. Gansecki *et al.*, 1996; Lanphere *et al.*, 2002; our new age for SBB) makes the isotopic trends through time (see Fig. 2) more complicated than previously thought. In particular, as there is an ~0·1–0·15 Myr time gap between the LCT and the first low-$\delta^{18}O$, higher $^{87}Sr/^{86}Sr_i$ UB lavas, there is no longer a need for a 'sudden' causal connection between caldera collapse and low-$\delta^{18}O$ magmas, or syn-collapse brine injection during caldera collapse. Taylor (1986), Hildreth *et al.* (1991) and Gansecki (1998) discussed the possibility of brine incorporation into the magma within porous stoped blocks sinking from the hydrated low-$\delta^{18}O$ roof. Although this interpretation is a possibility, we consider that the low-$\delta^{18}O$ UB rhyolites are more radiogenic as a result of their stronger hydrothermal alteration. Hydrothermal fluids could have leached and redeposited highly radiogenic Sr and Pb from the surrounding Archean country rocks and thus at greater fluid-to-rock ratios $\delta^{18}O$ and Sr (Pb) isotopes should anti-correlate. Likewise, the isotopic 'recovery' towards more normal $\delta^{18}O$ values seen between the UB and CPM magmas (Fig. 2; Hildreth *et al.*, 1984, 1991) simply indicates the involvement of less hydrothermally altered wall-rocks (in terms of $\delta^{18}O$).

Thus, radiogenic isotopic trends reflect isotopic differences between unrelated volumes of precursor rhyolites, variably altered by meteoric waters, and subsequent magma batches. There is no need for them to be derived from a single, long-lived, differentiating LCT magma reservoir.

Heat sources and thermal balances for rhyolite petrogenesis by remelting

Our finding of young post-LCT zircons in UB lavas that have LCT-like $\delta^{18}O$ values (Fig. 4) suggests that intrusion of the remaining LCT magma into the future magma generation zones of the UB units continued for tens of thousands of years after caldera collapse. The 0·5 Ma, low-$\delta^{18}O$ UB lavas were subsequently formed by remelting of the collapsed intra-caldera roof block (e.g. Bindeman & Valley, 2000). This work considers intruding basaltic magmas as the main source of heat for this remelting (Fig. 9), and we suggest that basaltic magma was able to gain access to intrude the collapsed intra-caldera block through open fractures developed in the solidified portions of the LCT batholith. In particular, basaltic magma could have intruded along the northern ring fracture of the Yellowstone caldera to generate the voluminous Canyon flow (Fig. 1).

However, the results of this work suggest that significant portions, if not all, of the LCT batholith were solidified and hydrothermally altered by the time of the CPM lava eruptions. The 0·25–0·1 Ma Central Plateau Member lavas may represent the products of remelting of a greater variety of pre-existing rocks, including Upper Basin rocks, as they contain zircons inherited from sources with diverse $\delta^{18}O$ values. However, the bulk of the Central Plateau Member lavas may perhaps represent products of the crystallized, hydrothermally altered LCT magma body,

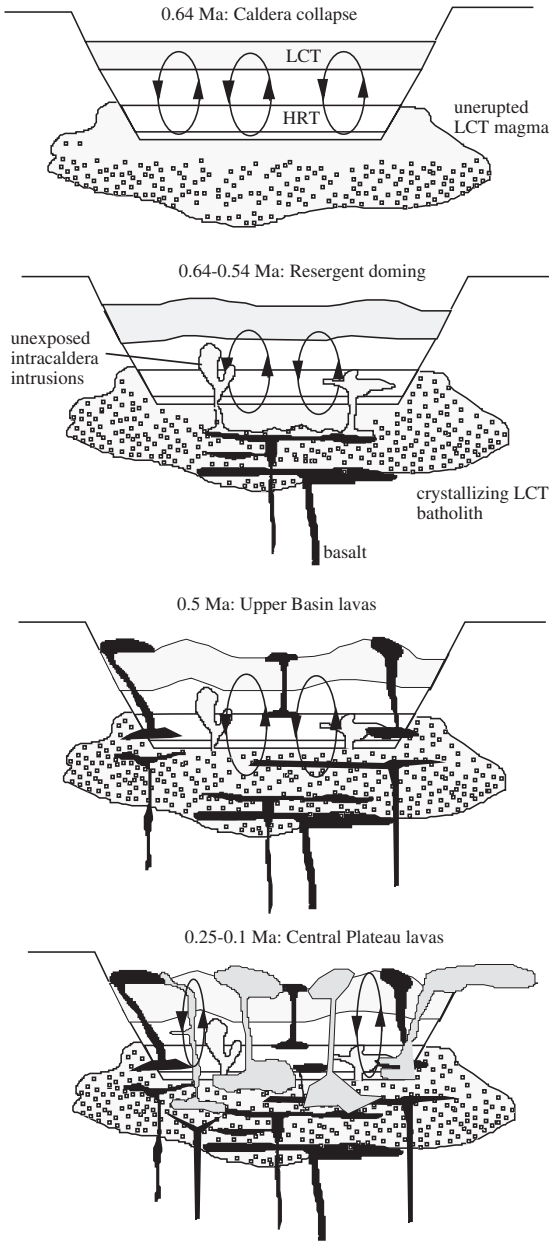

Fig. 9. Schematic illustration of the evolution of the Yellowstone caldera after the eruption of the Lava Creek Tuff (LCT) at 0·64 Ma. The remelting of small batches of previously crystallized magmas within the intra-caldera block, to form the youngest lavas, is shown from about 500 to 100 ka. Buried volcanic rocks and sub-volcanic intrusions are variably altered by heated low-$\delta^{18}O$ meteoric waters and thus have variably low bulk $\delta^{18}O$, whereas zircons retain their original U–Pb age and $\delta^{18}O$. High-$\delta^{18}O$ pre-caldera rocks (such as the intra-caldera HRT, solidified LCT batholith), and low-$\delta^{18}O$ post-LCT rocks of variable age are shown and contribute to the youngest volcanism at Yellowstone as evidenced by zircon recycling.

because these CPM magmas are close to the LCT in terms of their Sr, Nd, and Pb isotopic ratios (Hildreth *et al.*, 1991; Vazquez & Reid, 2002), but are isotopically distinct from the LCT with respect to oxygen isotopes. The voluminous CPM volcanism has led some researchers to consider it as representing the beginning of a fourth volcanic cycle at Yellowstone, representing either the leftover LCT magma or its mush, or a newly formed, single magma reservoir. We have argued above, based on the low and diverse $\delta^{18}O$ values of each magmatic unit, against a single large and evolving magma reservoir as the source of CPM lavas.

We propose that a process of progressive crustal remelting has continued since the last caldera collapse, caused by repeated intrusions of basaltic magma that kept the Yellowstone system alive (Fig. 9). In this study we put greater emphasis on the role of hot plume-derived basaltic magma intruded as sills and dikes into the solidifying LCT batholith (e.g. Annen & Sparks, 2002; Dufek & Bergantz, 2005). Previously, although accepting the basalt as the ultimate source of heat, we also considered the remaining LCT magma body as a heat source for remelting (e.g. Bindeman & Valley, 2000, 2001). Below we evaluate thermodynamic and thermal aspects of remelting caused by basaltic intrusions.

The important thermodynamic property of high-silica rhyolites is that they are compositionally close to the granitic minimum and have a fairly narrow (~50°C) melting interval (Tuttle & Bowen, 1958; Holtz, 1992; Brugger *et al.*, 2003). Melting and crystallization experiments on appropriate bulk compositions (altered high-silica rhyolitic tuffs with variable water contents) illustrate that 'bulk melting', whereby the proportions of melt change suddenly from zero to >75%, occurs slightly above the solidus (Fig. 10). Rapid remelting may occur with minimal supply of heat given: (1) the preheated near-solidus state of the intra-caldera rocks; (2) their glassy, low-crystallinity state that requires little latent heat of fusion; (3) the geometry of the intra-caldera down-dropped block (Fig. 9) that is inserted into the hot interior and thus is heated from the sides as well as the bottom with minimal dissipation of heat; (4) interstitial and structural water that may serve as a flux for melting. The diagram in Fig. 10 assumes 3 wt % water in the source rocks; the next 1 wt % of water will lower the solidus by ~30°C. Water may also facilitate effective heat transfer (e.g. Bachmann & Bergantz, 2006) and promote melting in specific parts of the crust with the right $P - T - X_{H_2O}$ composition. However, the kinetics of water retention and flow upon heating, and its role in promoting heat transfer and melting, needs to be modeled.

The amount of basalt required to generate ~40 km^3 of low-$\delta^{18}O$ UB rhyolites from a hydrothermally altered protolith that cooled below the solidus to ~500–600°C is estimated to be 10–40 km^3. This calculation is based on a 1·5 kJ/kg K heat capacity of basalt, 700°C basalt cooling

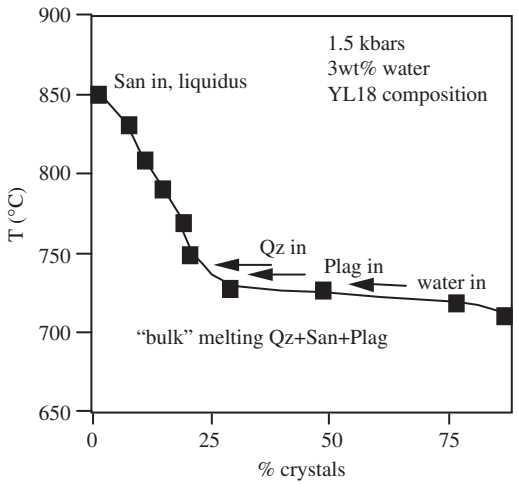

Fig. 10. Crystallization–melting relations for a high-silica rhyolite composition (Canyon flow of Yellowstone; sample YL18), at 1·5 kbar and 3 wt% water modeled with the MELTS program (Ghiorso & Sack, 1995). Crystallization starts with sanidine (San) at 850°C; this temperature can be called the 'liquidus'. Notice the small T difference between the 'liquidus' and 'solidus' as observed for many silicic magma compositions (Holtz, 1992; Tuttle & Bowen, 1958). When heated, 'bulk' melting of the rhyolite mineral assemblage occurs between 725 and 745°C, yielding 55% melt. If pressure, water concentrations, and bulk composition are slightly varied, it is possible to achieve the granitic minimum with $T_{solidus} = T_{liquidus}$, and a temperature change of 10–30°C may lead to >90% melting or crystallization.

from 1250°C liquidus to 550°C ambient temperature, and 400 kJ/kg latent heat of its crystallization, yielding a total of 1450 kJ/kg for basalt. It takes about 300–400 kJ/kg to melt a granitic rock by reheating it by 300°C and increasing the melt fraction by 50%, or only ~200 kJ/kg if the initial rock is already a glassy high-silica rhyolite with few crystals, and so little or no latent heat of fusion is required. At an assumed heat transfer efficiency (e.g. Dufek & Bergantz, 2005) of 20–40% for the pre-heated near-solidus intra-caldera block, the basalt can melt two to five times the volume of rhyolite. At high basaltic magma intrusion rates of 0·001 km^3/km^2 year, the generation of 40 km^3 of UB intra-caldera rhyolite would require only around 400–800 years and this time is not sufficiently long to dissolve and reprecipitate the inherited zircons, explaining the abundance of inherited cores. It would take 10 times longer to generate ~400 km^3 of CPM rhyolites, leading to proportionally longer rhyolitic magma residence time, and thus explaining the greater isotopic equilibrium in the CPM lavas.

CONCLUSIONS

(1) *In situ* ion microprobe analysis reveals greater $\delta^{18}O$ variability in the cores of zircons compared with an earlier laser fluorination study of the same samples, but the magnitude of the core-to-rim zoning is similar.

(2) Zircons from large-volume tuffs retain variable $\delta^{18}O$ in their cores. These values record segregation or inheritance from various sources, including partial melts from pre-existing low- and normal-$\delta^{18}O$ country rocks.
(3) Volcanism of Lava Creek Tuff-type magmas continued within the collapsed block from 0·1–0·15 Myr after caldera collapse until soon before the appearance of the low-$\delta^{18}O$ Upper Basin Member lavas.
(4) The youngest volcanic products of Yellowstone, the 0·25–0·1 Ma Central Plateau Member lavas, contain low-$\delta^{18}O$ zircon cores that are derived from remelting of the Upper Basin Member lavas. These voluminous post-caldera units continue the trend of remelting of intra-caldera rocks, rather than the evolution of a long-lived resident Lava Creek Tuff-like magma (mush).
(5) Sharp $\delta^{18}O$ isotopic profiles between cores and rims of zircons indicate a greater role for solution–reprecipitation compared with diffusion in achieving isotope exchange between minerals and melt.
(6) Intrusions of basaltic magma into a solidifying granitic batholith are probably responsible for spikes in post-caldera volcanism.
(7) The advocated processes may be applicable in other areas that do not have low-$\delta^{18}O$ magmas if there is no significant initial isotopic contrast between the local meteoric water and rocks.

ACKNOWLEDGEMENTS

We thank the University of Oregon and NSF (EAR-0537872) for material support of these analyses; NSF (EAR 03-19320, 05-16725), DOE (93ER14389) and the University of Wisconsin for purchase and support of the CAMECA ims-1280 ion microprobe, and salary support of ion microprobe staff; John Fournelle for help with imaging of zircons; Brian Hess for polishing samples; and Bill McIntosh and his group from New Mexico Tech for dating SBB sanidines by the Ar–Ar method. Chris Harris, Todd Feeley, and an anonymous reviewer are thanked for their constructive reviews, and Wendy Bohrson is thanked for editorial handling.

SUPPLEMENTARY DATA

Supplementary data for this paper are available at *Journal of Petrology* online.

REFERENCES

Anderson, A. T., Davis, A. M. & Lu, F. (2000). Evolution of Bishop Tuff rhyolitic magma based on melt and magnetite inclusions and zoned phenocrysts. *Journal of Petrology* **41**, 440–473.

Annen, C. & Sparks, R. S. J. (2002). Effects of repetitive emplacement of basaltic intrusions on thermal evolution and melt generation in the crust. *Earth and Planetary Science Letters* **203**, 937–955.

Bachmann, O. & Bergantz, G. W. (2004). On the origin of crystal-poor rhyolites: extracted from batholithic crystal mushes. *Journal of Petrology* **45**, 1565–1582.

Bachmann, O. & Bergantz, G. W. (2006). Gas percolation in upper-crustal silicic crystal mushes as a mechanism for upward heat advection and rejuvenation of near-solidus magma bodies. *Journal of Volcanology and Geothermal Research* **149**, 85–102.

Bacon, C. R. & Lowenstern, J. B. (2005). Late Pleistocene granodiorite source for recycled zircon and phenocrysts in rhyodacite lava at Crater Lake, Oregon. *Earth and Planetary Science Letters* **233**, 277–293.

Bacon, C. R., Adami, L. H. & Lanphere, M. A. (1989). Direct evidence for the origin of low-$\delta^{18}O$ silicic magmas: quenched samples of a magma chamber's partially-fused granitoid walls, Crater Lake, Oregon. *Earth and Planetary Science Letters* **96**, 199–208.

Baker, D. R. (1991). Interdiffusion of hydrous dacitic and rhyolitic melts and the efficacy of rhyolite contamination of dacitic enclaves. *Contributions to Mineralogy and Petrology* **106**, 462–473.

Bindeman, I. N. (2003). Crystal sizes in evolving silicic magma chambers. *Geology* **31**, 367–370.

Bindeman, I. N. & Valley, J. W. (2000). The formation of low-$\delta^{18}O$ rhyolites after caldera collapse at Yellowstone, Wyoming, USA. *Geology* **28**, 719–722.

Bindeman, I. N. & Valley, J. W. (2001). Low-$\delta^{18}O$ rhyolites from Yellowstone: magmatic evolution based on analyses of zircons and individual phenocrysts. *Journal of Petrology* **42**, 1491–1517.

Bindeman, I. N. & Valley, J. W. (2003). Rapid generation of both high- and low-delta O-18 large-volume silicic magmas at the Timber Mountain/Oasis Valley caldera complex, Nevada. *Geological Society of America Bulletin* **115**, 581–595.

Bindeman, I. N., Valley, J. W., Wooden, J. L. & Persing, H. M. (2001). Post-caldera volcanism: *in situ* measurement of U–Pb age and oxygen isotope ratio in Pleistocene zircons from Yellowstone caldera. *Earth and Planetary Science Letters* **189**, 197–206.

Bindeman, I. N., Watts, K. E., Schmitt, A. K., Morgan, L. A. & Shanks, P. W. C. (2007). Voluminous low-$\delta^{18}O$ magmas in the late Miocene Heise volcanic field, Idaho: implications for the fate of Yellowstone hotspot calderas. *Geology* **35**, 1019–1022.

Brugger, C. R., Johnston, A. D. & Cashman, K. V. (2003). Phase relations in silicic systems at one-atmosphere pressure. *Contributions to Mineralogy and Petrology* **146**, 356–369.

Charlier, B. L. A., Wilson, C. J. N., Lowenstern, J. B., Blake, S., Van Calsteren, P. W. & Davidson, J. P. (2005). Magma generation at a large hyperactive silicic volcano (Taupo New Zealand) revealed by U–Th and U–Pb systematics in zircons. *Journal of Petrology* **46**, 3–32.

Christiansen, R. L. (1989). The Yellowstone Plateau volcanic field. In: Field Excursions to Volcanic Terranes in the Western United States, Volume II: Cascades and Intermountain West. New Mexico Bureau of Mines and Mineral Resources, Memoirs **47**, 137–153.

Christiansen, R. L. (2001). The Quaternary and Pliocene Yellowstone Plateau Volcanic Field of Wyoming, Idaho, and Montana. US Geological Survey, Professional Papers **729-G**, 145 pp.

Doe, B. R., Leeman, W. P., Christiansen, R. L. & Hedge, C. E. (1982). Lead and strontium isotopes and related trace elements as genetic tracers in the Upper Cenozoic rhyolite–basalt association of the Yellowstone Plateau volcanic field. *Journal of Geophysical Research* **87**, 4785–4806.

Dufek, J. & Bergantz, G. W. (2005). Lower crustal magma genesis and preservation: A stochastic framework for the evaluation of basalt–crust interaction. *Journal of Petrology* **46**, 2167–2195.

Fournelle, J., Bindeman, I. N., Donovan, J. D. & Valley, J. W. (2000). Quantitative EMPA mapping of zircons from Yellowstone. *EOS Transactions, American Geophysical Union* **81** (Spring Meeting), 26–27.

Friedman, I., Lipman, P. W., Obradovich, J. D., Gleason, J. D. & Christiansen, R. L. (1974). Meteoric water in magmas. *Science* **184**, 1069–1072.

Gansecki, C. A. (1998). $^{40}Ar/^{39}Ar$ geochronology and pre-eruptive geochemistry of the Yellowstone Plateau volcanic field rhyolites. PhD thesis, Stanford University, Stanford, CA, 213 pp.

Gansecki, C. A., Mahood, G. A. & McWilliams, M. O. (1996). $^{40}Ar/^{39}Ar$ geochronology of rhyolites erupted following collapse of the Yellowstone caldera, Yellowstone Plateau volcanic field: implications for crustal contamination. *Earth and Planetary Science Letters* **142**, 91–107.

Ghiorso, M. S. & Sack, R. O. (1995). Chemical mass-transfer in magmatic processes IV: A revised and internally-consistent thermodynamic model for the interpolation and extrapolation of liquid–solid equilibria in magmatic systems at elevated temperatures and pressures. *Contributions to Mineralogy and Petrology* **119**, 197–212.

Harrison, T. M. & Watson, E. B. (1983). Kinetics of zircon dissolution and zirconium diffusion in granitic melts of variable water-content. *Contributions to Mineralogy and Petrology* **84**, 66–72.

Hildreth, W., Christiansen, R. L. & O'Neil, J. R. (1984). Catastrophic isotopic modification of rhyolitic magma at times of caldera subsidence, Yellowstone Plateau Volcanic Field. *Journal of Geophysical Research* **89**, 8339–8369.

Hildreth, W., Halliday, A. N. & Christiansen, R. L. (1991). Isotopic and chemical evidence concerning the genesis and contamination of basaltic and rhyolitic magmas beneath the Yellowstone Plateau Volcanic Field. *Journal of Petrology* **32**, 63–138.

Holtz, F. (1992). Effects of H_2O on liquidus phase-relations in the haplogranite system at 2 and 5 kbar. *American Mineralogy* **77**, 1223–1241.

Hoskin, P. W. O. & Schaltegger, U. (2003). The composition of zircon and igneous and metamorphic petrogenesis. In: Hanchar, J. M. & Hoskin, P. W. O. (eds) *Zircon. Mineralogical Society of America, Reviews in Mineralogy and Geochemistry* **53**, 27–62.

Kelly, J. L., Fu, B., Kita, N. T. & Valley, J. W. (2007). Optically continuous silcrete cements of the St. Peter Sandstone: Oxygen isotope analysis by ion microprobe and laser fluorination. *Geochimica et Cosmochimica Acta* **71**, 3812–3832.

Kempe, U., Gruner, T., Nasdala, L. & Wolf, D. (2000). Relevance of cathodoluminescence for the interpretation of U–Pb zircon ages, with an example of an application to a study of zircons from the Saxonian Granulite Complex, Germany. In: Pagel, M., Barbin, V., Blanc, P. & Ohnenstetter, D. (eds) *Cathodoluminescence in Geosciences*. Berlin: Springer, Berlin, pp. 415–455.

Kita, N. T., Ikeda, Y., Togashi, S., Liu, Y. Z., Morishita, Y. & Weisberg, M. K. (2004). Origin of ureilites inferred from a SIMS oxygen isotopic and trace element study of clasts in the Dar al Gani 319 polymict ureilite. *Geochimica et Cosmochimica Acta* **68**, 4213–4235.

Kita, N. T., Ushikubo, T., Fu, B., Spicuzza, M. J. & Valley, J. W. (2007). Analytical developments on oxygen three isotope analyses using a new generation ion microprobe, ims-1280. *Lunar and Planetary Science* **XXXVIII**, abstract 1981.

Lanphere, M. A., Champion, D. E., Christiansen, R. L., Izett, G. A. & Obradovich, J. D. (2002). Revised ages for tuffs of the Yellowstone Plateau volcanic field: Assignment of the Huckleberry Ridge Tuff to a new geomagnetic polarity event. *Geological Society of America Bulletin* **114**, 559–568.

Leeman, W. P. (1982). Rhyolites of the Snake River Plain–Yellowstone Plateau Province, Idaho and Wyoming: A summary of petrogenic models. In: Bonnichsen, B. & Breckenridge, R. M. (eds) *Cenozoic Geology of Idaho. Idaho Bureau of Mines and Geology Bulletin* **26**, 193–202.

Lu, F. Q., Anderson, A. T. & Davis, A. M. (1992*a*). Melt inclusions and crystal–liquid separation in rhyolitic magma of the Bishop Tuff. *Contributions to Mineralogy and Petrology* **110**, 113–120.

Lu, F. Q., Anderson, A. T. & Davis, A. M. (1992*b*). New and larger sanidine/melt partition coefficients for Ba and Sr as determined by ion microprobe analyses of melt inclusions and their sanidine host crystals. *Geological Society of America, Abstracts with Programs*, **24**, A44.

Mahood, G. & Hildreth, W. (1983). Large partition-coefficients for trace-elements in high-silica rhyolites. *Geochimica et Cosmochimica Acta* **47**, 11–30.

Marsh, B. D. (1981). On the crystallinity, probability of occurrence, and rheology of lava and magma. *Contributions to Mineralogy and Petrology* **78**, 85–98.

Morgan, L. A. & McIntosh, W. C. (2005). Timing and development of the Heise volcanic field, Snake River Plain, Idaho, western USA. *Geological Society of America Bulletin* **117**, 288–306.

Obradovich, J. D. (1992). Geochronology of the Late Cenozoic volcanism of Yellowstone National Park and adjoining areas, Wyoming and Idaho. *US Geological Survey, Open-File Report* **92-408**, 1–45.

Page, F. Z., Ushikubo, T., Kita, N. Y., Riciputi, L. R. & Valley, J. W. (2007). High precision oxygen isotope analysis of picogram samples reveals 2-μm gradients and slow diffusion in zircon. *American Mineralogist* **92**, 1772–1775.

Peck, W. H., Valley, J. W. & Graham, C. M. (2003). Slow oxygen diffusion rates in igneous zircons from metamorphic rocks. *American Mineralogist* **88**, 1003–1014.

Smith, R. L. (1979). Ash-flow magmatism. In: Chapin, C. E. & Elston, W. E. (eds) Ash Flow Tuffs. *Geological Society of America, Special Papers* **180**, 5–27.

Taylor, H. P., Jr (1986). Igneous rocks: II. Isotopic case studies of circumpacific magmatism. In: Valley, J. W., Taylor, H. P., Jr & O'Neil, J. R. (eds) *Stable Isotopes in High Temperature Geological Processes. Mineralogical Society of America, Reviews in Mineralogy* **16**, 273–316.

Tuttle, O. F. & Bowen, N. (1958). Origin of Granite in the Light of Experimental Studies in the System Ab–Or–Qz–H_2O. Geological Society of America, Memoirs **74**.

Valley, J. W. (2003). Oxygen isotopes in zircon. In: Hanchar, J. M. & Hoskin, P. W. O. (eds) *Zircon. Mineralogical Society of America, Reviews in Mineralogy and Geochemistry* **53**, 343–385.

Valley, J. W., Bindeman, I. N. & Peck, W. H. (2003). Empirical calibration of oxygen isotope fractionations in zircon. *Geochimica et Cosmochimica Acta* **67**, 3257–3266.

Vazquez, J. A. & Reid, M. R. (2002). Time scales of magma storage and differentiation of voluminous high-silica rhyolites at Yellowstone caldera, Wyoming. *Contributions to Mineralogy and Petrology* **144**, 274–285.

Watson, E. B. (1996). Dissolution, growth and survival of zircons during crustal fusion: Kinetic principles, geological models and implications for isotopic inheritance. *Transactions of the Royal Society of Edinburgh: Earth Sciences* **87**, 43–56.

Watson, E. B. & Cherniak, D. J. (1997). Oxygen diffusion in zircon. *Earth and Planetary Science Letters* **148**, 527–544.

Watson, E. B. & Harrison, T. M. (1983). Zircon saturation revisited: temperature and compositional effects in a variety of crustal magma types. *Earth and Planetary Science Letters* **64**, 295–304.

Watson, E. B. & Liang, Y. (1995). A simple model for sector zoning in slowly grown crystals: implications for growth rate and lattice diffusion, with emphasis on accessory minerals in crustal rocks. *American Mineralogist* **80**, 1179–1187.

Wicks, C. W., Thatcher, W., Dzurisin, D. & Svarc, J. (2006). Uplift, thermal unrest and magma intrusion at Yellowstone caldera. *Nature* **440**, 72–75.

Zhang, Y. X., Walker, D. & Lesher, C. E. (1989). Diffusive crystal dissolution. *Contributions to Mineralogy and Petrology* **102**, 492–513.